Integrated design optimization of heat exchangers for additive manufacturing in electrified automotive, aerospace and marine applications

Applied Thermal Engineering 305 (2026) 132753

Contents lists available at ScienceDirect

Applied Thermal Engineering

journal homepage: www.elsevier.com/locate/ate

Research Paper

Integrated design optimization of heat exchangers for additive manufacturing in electrified automotive, aerospace and marine applications ☆

S. Favre [a], D. Di Blasio [b,*], T. Fletcher [b], E. Brusa [a], C. Delprete [a]

[a] Politecnico di Torino, Corso Duca degli Abruzzi, 24, Torino, 10129 TO, Italy
[b] University of Bath, Claverton Down, Bath, BA2 7AY, United Kingdom

ARTICLE INFO

Keywords:
Transport
Electrification
Fuel cell
Heat exchanger
Additive manufacturing
Design
Optimization

ABSTRACT

The design optimization of heat exchangers (HE) is a key enabler for addressing the substantial amounts of low-grade waste heat generated by proton exchange membrane (PEM) fuel cells in transport electrification. Concurrently, advances in Additive Manufacturing (AM) technology introduce new opportunities for unprecedented HE geometries, supporting enhanced heat transfer, compactness, and reduced mass. This study proposes a structured optimization framework, based on validated methodologies, to support the rapid conceptualization and refinement of compact cross-flow heat exchangers compatible with Selective Laser Melting (SLM). The presented technique is applied to a literature case, achieving up to 50% mass savings and 31% improved heat transfer. Subsequently, it is extended to a nominal 100 kW cross-flow air radiator to maximize its thermal effectiveness, while minimizing component mass with respect to automotive, aerospace, and marine applications. The methodology quantifies how different optimization goals and application constraints influence the global and internal dimensions of the solution. Results exhibit that rectangular channels reduce overall component mass by approximately 33% and 13% compared to circular and combined circular–rectangular configurations. Circular channels show a compactness improvement on the range of 10%–20% with respect to rectangular ducts, increasing up to 30% for hybrid configurations. A dynamic simulation model completes the assessment by ranking non-dominated solutions using an application-specific coefficient of performance (CoP). Findings provide guidelines for future modular propulsion system design, indicating that mass-minimized designs are generally best suited for automotive and aerospace systems, whereas balanced mass–thermal optimization targets yield the highest CoPs for marine applications.

1. Introduction

Recent studies on pollutant emissions reduction and global warming mitigation [1,2] highlight how decarbonizing the transport sector remains a key step towards achieving the net-zero transition. Powertrain electrification emerges as a strong candidate to meet increasingly stringent international emission targets [3] and local regulations [4,5], and is currently supported by several industrial initiatives and partnerships across the automotive [6,7], marine [8–11], and aerospace [12, 13] technical domains. Nonetheless, several challenges remain that hinder the widespread adoption of electrified transport, particularly regarding the performance and thermal management of state-of-the-art energy storage and conversion devices. These challenges are especially pronounced in fuel-cell systems [14]. Low-temperature proton exchange membrane fuel cells (LT-PEMFCs) are amongst the most widely deployed technologies [15], typically operating at relatively low temperatures (60 °C to 80 °C) and modest electrical efficiencies of approximately 50% [16]. Accordingly, these systems are bound to generate a substantial amount of low-grade waste heat, posing significant challenges to conventional radiator-based cooling. Enhanced heat dissipation is therefore essential for the widespread adoption of fuel cells in automotive, aerospace, and marine applications [17–20], motivating the development of refined heat exchanger (HE) design, combining increased thermal performance, compactness, and efficiency.

Contemporarily, recent advances in Additive Manufacturing (AM) [21–23] have significantly expanded the design freedom available for heat exchanger development, enabling complex architectures that are impractical or impossible to realize using conventional manufacturing

☆ This publication is part of the project PNRR-NGEU which has received funding from the Italian Ministry of University and Research (MUR) - DM 352/2022 (CUP n°E12B22000560006)

* Corresponding author.
E-mail addresses: stefano.favre@polito.it (S. Favre), ddb35@bath.ac.uk (D. Di Blasio).

https://doi.org/10.1016/j.applthermaleng.2026.132753
Received 8 April 2026; Received in revised form 5 July 2026; Accepted 6 August 2026
Available online 28 August 2026

Nomenclature

Greek symbols

Δp	Pressure drop
δ_{bl}	Boundary layer thickness
ϵ	Equivalent sand–grain roughness
η	Efficiency
μ	Dynamic viscosity
ϕ	Ratio of mean to initial temperature difference
ρ	Density
σ	Porosity (HE)
ε	Thermal effectiveness

Latin symbols

$\dot{m}$	Mass flow rate
$\overline{h}$	Convective heat transfer coefficient (average)
A	Area
a	Hot fluid dimensionless thermal capacity ratio (Eq. (2))
B	Base (length)
b	Cold fluid dimensionless thermal capacity ratio (Eq. (2))
C	Thermal capacity
c_p	Specific heat (const. pressure)
D	Diameter
D_{hyd}	Hydraulic diameter
f	Objective function (fitness)
f'	Normalized objective function (fitness)
f_D	Darcy–Weisbach friction factor
G	Mass flux rate
H	Height
H_w	Wall thickness
k	Thermal conductivity
K_{contr}	Contraction loss coefficient
K_{exp}	Expansion loss coefficient
k_f	Objective function normalization factor
K_p	AM pressure drop penalty factor
L	Length - cold fluid direction
l_{th}	Dimensionless thermal length
m	Mass
m_{fin}	Dimensionless fin parameter of Eq. (9)
N_{fin}	Number of fins
n_{layers}	Number of layers
n_{plt}	Number of plates
Nu	Nusselt number
P	Perimeter
p	Pressure
Pr	Prandtl number
q	Heat transfer rate
R	Thermal resistance
Ra	Arithmetic mean directional roughness
Re	Reynolds number
T	Temperature
U	Global heat transfer coefficient
u	Velocity
V	Volume
W	Length - hot fluid direction

Superscripts

$target$	Optimization target

Subscripts

1	Section 1 (upstream HE inlet)
2	Section 2 (downstream HE inlet)
3	Section 3 (upstream HE outlet)
4	Section 4 (downstream HE outlet)
air	Air
$base$	Base surface (between two fins)
$chan$	Channel
$cond$	Conductive
$conv$	Convective
$corr$	Corrected
cs	Cross section (or cross-sectional)
c	Cold side/cold fluid
$e-motor$	Electric motor
eff	Thermal effectiveness-related
FC	Fuel cell
fin	Fin
HE	Heat exchanger
hyd	Hydraulic
h	Hot side/hot fluid
lam	Laminar
$mass$	Mass-related
out	Out/outlet
plt	Plate
s	Structure (dry HE)
th	Thermal
$turb$	Turbulent
w	Wall

Other symbols

AM	Additive Manufacturing
ANN	Artificial Neural Network
CFD	Computational Fluid Dynamics (simulation)
CoP	Coefficient of Performance
DoE	Design of Experiments
FEM	Finite Element Method
GA	Genetic Algorithm
HE	Heat exchanger
MOGA	Multi-Objective Genetic Algorithm
SLM	Selective Laser Melting
TO	Topology optimization
WCS	Worst-Case Scenario

techniques. This emerging capability strongly complements the growing demands of transport electrification and decarbonization, where lightweight, compact, and highly efficient thermal management systems are increasingly required. In particular, Fawaz et al. [24] emphasize that the integration of advanced optimization methods with AM is essential to fully harness the design freedom enabled by these processes. This perspective is further supported by the comprehensive review of Kaur et al. [22], which summarizes recent progress in AM-enabled heat exchanger development, highlighting the emergence of increasingly complex and better-performing architectures.

Similarly, Careri et al. [23] identify a strong synergy between AM and optimization-driven design, particularly in aerospace applications, where stringent requirements for weight reduction, compactness, and thermal performance are critical. As design freedom expands through Additive Manufacturing, computationally efficient modelling and optimization methods become increasingly critical. Faster simulation tools enable the exploration of larger design spaces, allowing optimization algorithms to identify improved trade-offs between thermal performance, mass, compactness, and manufacturability. Consequently, numerical design frameworks and advanced optimization routines emerge as a timely research direction, reducing prototyping costs and accelerating development cycles.

According to Fawaz et al. [24], design optimization methods can be classified into three main categories: size, shape, and topology optimizations (TO). Size optimization represents the simplest approach and focuses on the adjustment of predefined feature dimensions without modifying the overall geometry. Shape optimization extends these concepts by enabling the selection and refinement of a prescribed set of geometric features. Finally, topology optimization employs more advanced techniques to generate entirely new layouts with minimal geometric constraints. As a result, TO offers significant potential for performance improvement, but typically demands substantially higher computational costs.

Sensitivity analyses and parametric studies represent the most straightforward approaches to size and shape optimization. They provide early insight into the influence of individual design features on component performance. However, they are typically not automated and require active user intervention for both result evaluation and design selection. Moreover, when multiple design variables and objectives are involved, these methods are generally unable to efficiently identify the true optimal solution. Northcutt and Mudawar [25] present an extensive parametric study aimed at maximizing heat transfer in a finned microchannel air–fuel heat exchanger module. The study independently varies the channel and fin widths and heights to identify design trends associated with enhanced thermal performance, which increases significantly as the air-side channel width is reduced to approximately 0.1 mm and the channel height is increased to around 2.5 mm. Similar, albeit less pronounced, trends are observed on the liquid side of the heat exchanger module. Likewise, the work of Rasouli et al. [26] proposes the preliminary parametric analysis of a novel 3D-printed polymeric HE to rapidly assess the design trade-offs between thermal effectiveness and pressure drops associated with the channels' length and width. The study yields a set of feasible solutions without converging to a single optimal configuration and demonstrates that thermal effectiveness in excess of 80% can be achieved for channel widths between 1.6 mm to 1.8 mm and channel lengths between 190 mm to 250 mm, while maintaining air pressure drops below 100 Pa.

Several studies combine parametric optimization with computational fluid dynamics (CFD) simulations to investigate complex heat exchanger geometries, exploiting the simplicity of parametric methods to offset the high computational cost of individual simulations. An early example is provided by Lee et al. [27] and addresses the optimization of a printed-circuit counterflow heat exchanger with zig-zag channels by performing 20 preset RANS simulations spanning different channel pitches, wavelengths, and angles. The resulting dataset is then used to construct a Response Surface Analysis (RSA), later optimized through a Genetic Algorithm (GA) for the efficient identification of near-optimal configurations. The work of Modi et al. [28] adopts a similar methodology, analysing four tube-fin winglet configurations via two-dimensional CFD to maximize a j/f heat transfer-to-pressure drop ratio, where j is the thermal Colburn j-factor and f the hydraulic Fanning f-factor. Lee et al. [29] further extended this framework by conducting a campaign of three-dimensional simulations across twenty-one wavy fin-tube HE configurations, optimizing a $j/f^{1/3}$ performance metric with respect to three key geometric parameters: fin height, wavelength, and fin pitch. Conversely, Arjmandi et al. [30] employ a structured Design of Experiments (DoE) to frame the parametric analysis of twenty tridimensional simulations of vortex generators in double-pipe HEs, tracing approximate response surfaces for the features' angle and pitch-to-length ratio. These maps are subsequently used in combination with a Response Surface Methodology (RSM) to enhance the parametric analysis and simplify the selection of the final design, allowing to numerically identify near-optimal configurations.

Recent studies suggest integrating structured DoE with more advanced techniques, such as Artificial Neural Networks (ANNs), enabling more accurate response mapping and more impactful optimization with numerous design parameters. Abbasi et al. [31] exemplify this approach by conducting a campaign of thirty-six CFD simulations of different porous baffles for shell-and-tube HEs comparing multiple baffle numbers, thicknesses, and free-stream angles. The resulting dataset is then used to train and validate a five-layer artificial neural network (ANN), which is coupled with a Genetic Algorithm (GA) to optimize the baffle geometry and identify the Pareto front describing the trade-off between heat transfer enhancement and pressure drop. The work of Sarangi et al. [32] extends this methodology to the optimization of vortex generators in fin-tube HEs, simulating 125 winglet configurations to train an ANN and subsequently performing a comparable GA-driven design optimization.

In practice, ANNs introduce a powerful tool for high-resolution performance mapping and optimization, usually outperforming traditional RSM. Nonetheless, while these methods are numerically efficient in use, they require a significant computational upfront effort, involving case simulation, network training, and final optimization. Moreover, ANN training must be handled with care to prevent issues such as data overfitting, anomaly sensitivity, limited generalization, and low interpretability, as outlined in the review by Zou et al. [33], while the scalability of these methods remains uncertain and the subject of ongoing research [34], with most studies being restricted to the optimization of only two to three design parameters [31,32,35].

The fields of electronics cooling and thermoelectric generation provide notable examples of response surface mapping applied to thermal design optimization. The work of Kleiner et al. [36] presents an early study on the enhancement of conventional finned-plate heat sinks, employing computationally inexpensive physics-based models to systematically vary channel and fin widths and generate detailed performance maps. These maps capture the effects of the geometric parameters on thermal resistance, pressure drop, and pumping power, enabling the identification of an optimal design. Pujol et al. [37] expand on this approach to pursue the optimization of a thermoelectric generator, balancing heat transfer enhancement against pressure drop to maximize net power output. In both cases, however, the analysis is limited to only two design variables, as computational costs increase rapidly with dimensionality while the interpretability of performance maps deteriorates. Zhuang et al. [38] address these limitations by employing an enumeration-based optimization approach that autonomously explores the design space by progressively varying each design parameter with a fixed step size until predefined performance criteria are satisfied. Applied to an innovative rhombus-fractal heat sink characterized by three principal design variables, the method manages the higher optimization complexity, but remains computationally demanding, while its preset stopping criteria do not guarantee identification of the global optimum.

More efficient optimization techniques also exist and can achieve rapid convergence without extensive parameter sweeps. The work of Shuja [39] presents an analytical optimization approach based on the governing heat transfer and fluid flow equations rather than an explicit exploration of the design space. By deriving and minimizing a thermal cost function, the study directly identifies the optimal design parameters, avoiding the computational burden associated with exhaustive parametric searches. Such optimization processes can then be further automated through gradient-based methods. For example, Culham and Muzychka [40] employ an entropy-generation minimization strategy to optimize the fin height, fin width, airflow velocity, and number of fins of a conventional heat sink. By iteratively following the local gradient of the objective function, the method converges rapidly towards a nearby numerical optimum. However, such approaches generally struggle to identify the global optimum in the presence of complex response surfaces containing multiple local minima and may exhibit sensitivity to initial design point selection and numerical instabilities [41]. Consequently, their effectiveness tends to diminish as the dimensionality and complexity of the optimization problem increase.

When addressing the optimization of thermal components characterized by a large number of design variables, Genetic Algorithms (GAs) emerge as a particularly effective tool, especially for exploring complex, highly nonlinear, design spaces and addressing multi-objective optimization problems. The work of Lim et al. [42] exemplifies this concept by implementing a GA-based multi-objective optimization (MOGA) to refine up to five design parameters and maximize the heat transfer in a conventional bare tube HE. The study traces the Pareto-optimal frontiers of the device's heat transfer and air-side pressure drops, comparing the results with those from existing louvred fin HEs. Similarly, Li et al. [43] apply a MOGA to enhance the thermo-hydraulic performance of a serrated fin compact HE through the refinement of four fin size parameters and the HE length. The study proposes employing the entransy theory, which quantifies the system heat-transfer potential $E_{hv} = \frac{1}{2} m c_v T^2$, to derive and minimize an entransy-dissipation-based thermal resistance $R_{hv} = E_{hv}/Q^2$. The approach is shown to yield improved non-dominated solutions compared to using conventional Colburn j and Fanning f factors. The work of Garcia et al. [44], instead, addresses the multi-objective refinement of a microchannel HE by applying a linear scalarisation of the optimization problem, according to Eq. (1):

$$f(x) = \sum_{i=1}^{n} q_i f_i' \quad \text{with} \quad \sum q_i = 1 \tag{1}$$

where f_i' denotes the normalized objective function f_i. This scalarisation transforms the original multi-objective problem into a single-objective optimization task, allowing the maximization of component performance relative to occupied volume in Ref. [44]. The Pareto-optimal frontier is then reconstructed through a sequence of scalarized optimizations, in which the weighting coefficients q_i are varied from 0 to 1 in increments of 0.05, with each non-dominated solution corresponding to a particular weighted combination of the normalized objective functions. The work by Arie et al. [45] avoids running multiple scalarized optimizations by adopting a hybrid-MOGA approach to optimize up to 12 design variables in a novel manifold-microchannel HE for AM. The optimization simultaneously maximizes thermo-hydraulic performance while minimizing component mass, enabling a comprehensive redesign of the heat exchanger layout rather than a mere refinement of channel geometries. The resulting optimized design achieves up to a 60% increase in gravimetric heat transfer density compared with conventional solutions, while suggesting that additional performance gains could be realized as AM technologies enable thinner microchannel walls, fins, and manifold features. Nevertheless, consistent with findings reported elsewhere in the literature [22,23,46], the study highlights the persistent tendency of current numerical models to underestimate pressure losses in additively manufactured heat exchangers. Recent work by Das et al. [47] expands the scope of optimization beyond the thermo-hydraulic performance by combining simplified physics-based thermal, hydraulic, mechanical, and structural models with preliminary cost analyses to perform a comprehensive genetic-algorithm-based techno-economic optimization of an AM plate-pin heat exchanger. This contribution reflects an emerging trend in the field, in which optimization frameworks are evolving from individual features refinements towards integrated engineering tools capable of simultaneously addressing performance, manoeuvrability, application and economic constraints.

Mekky et al. [48], instead, extend the use of GA-driven optimization to the refinement of up to 2500 parameters, enabling a preliminary topological optimization of serrated-fin profiles in compact HE. Each parameter defines a single mesh point as either solid or fluid, and is iteratively adjusted to maximize a $Q/dp^{1/3}$ ratio estimated via CFD simulations, resulting in a 45% performance increase in single-fin domains and a 89% improvement for two fin domains. Petrovic et al. [49] also employ Finite Element Method (FEM) to progressively refine the fin profiles of serrated-fin HEs, introducing mesh adaptation after every iteration to improve resolution at the interface between liquid and feature surfaces. The analysis exploits periodicity at the design space boundaries to restrict the optimization to a 2D refinement of a narrow core section. The resulting topology is then extended to the full scale component and its performance verified against 3D CFD simulations and experimental measurement, following fabrication by AM. A similar approach is presented in the works of Moon et al. [50,51], in which TO based on GA logic are applied to the refinement of internal fin geometries in double-pipe HEs cross sections. The study leverages radial symmetries within the pipe-fin layout to minimize computational costs of the 2D cross-section FEM simulations, replicating the geometry along the pipe polar coordinates and length. In particular, numerical and experimental results from Ref. [51] demonstrate substantially increased performance, comparable to brazed plate HE designs.

The work of Feppon et al. [52] further integrates evolutionary algorithms with advanced tools for topological optimization, combining meshed and level-set domain representations solved via FEM. It first applies the method to the relatively simple optimization of a single-flow finned-tube HE using two-dimensional CFD simulations, later extending it to more complex 2D and 3D multi-flow configurations. The study highlights how the new methodology significantly improves accuracy and robustness of the TO, particularly at the design interfaces, but remains computationally expensive, with the 3D optimizations requiring up to 8 days of continuous processing for the refinement of a relatively small design space. Recent work by Sun et al. [53] extends the application of topology optimization (TO) to larger counterflow heat exchanger designs by restricting the optimization domain to only 1/100 of the total channel length and subsequently replicating the resulting unit cell throughout the exchanger. The proposed methodology demonstrates improvements of up to 25% in heat transfer rate and power density compared with conventional designs. However, the periodic replication of the optimized geometry does not fully account for the progressive variation of fluid properties along the flow path, with the authors suggesting that homogenization-based TO approaches could yield further performance gains by explicitly incorporating these spatial variations into the optimization process. Accordingly, TO offers significant potential for performance improvements, but remains constrained to substantial computational costs even for small design spaces. Additionally, they still face challenges in effectively addressing interface flow behaviour, multi-stream configurations, and multi-objective optimizations.

Overall, the literature reports a broad spectrum of optimization strategies applied across several active research areas, highlighting the increasing interest in advanced heat exchanger design methodologies. A summary of the principal approaches, including their key features, advantages, and limitations, is provided in Table 1. AM is consistently identified as a key enabler for more effective design, synergizing with optimization techniques to overcome the geometric constraints limiting traditional heat sink and heat exchanger design.

Nevertheless, most studies remain focused on the optimization of one or a limited number of internal heat-exchanger features, primarily targeting enhanced thermo-hydraulic performance through metrics such as j/f, $j/f^{1/3}$, or $Q/dp^{1/3}$. Conversely, fewer contributions address the global redesign of the heat exchanger architecture or explicitly consider the minimization of component mass and volume, despite their relevance in applied thermal engineering applications, particularly in aerospace. Furthermore, limited attention has been devoted to optimization frameworks incorporating application-specific requirements, such as meeting a prescribed heat transfer target, satisfying geometric constraints, or maintaining pressure-drop limits. Only a few

Table 1
Principal methodologies applied to HE design optimization.

Methodology	Features	Computational costs	Parameters	Objectives	Refs.
Parametric analyses	Based on *lumped models* or *CFDs*, simple, and intuitive, but require active user intervention for result evaluation and design selection.	Very low (higher for CFDs)	1–2	Single: physical property or ratio	Lumped: [25,26] CFD: [28,29]
Response surface methodologies (+DoE)	Based on *lumped models* or *CFDs*, simple, and intuitive, can be integrated with ANN, GA, and Gradient-Methods for automated optima identification, but only support low dimensionality.	Low (higher for CFDs)	1–2	Single: physical property or ratio	Lumped: [27,36,37,39] CFD: [30]
Enumeration methods	Automated and simple, but do not guarantee global optimum identification.	Low, higher with dimensionality, design space, and resolution	2–3	Multiple: stops when performance targets are met	[38]
Gradient-based methods	Automated with rapid convergence to local optimum, but require careful setting, are bound to low dimensionality, and do not guarantee global optimum identification.	Low	3–4	Single: physical property or ratio	[40]
Artificial neural networks	Can support accurate complex shapes analysis when trained from CFD data and supports multi-objective optimization when combined with GA, but can be subject to numerical overfitting and generalization.	High upfront, low once trained	2–3 (4+ future)	Multiple: physical property or ratio	[31,32,34,35]
Genetic algorithms	*Scalarized*: automated, flexible, and robust, they simplify any multi-objective problem into a single-target optimization, but can be computationally expensive if used to trace a Pareto fronts via multiple runs.	Moderate to high	2–4+	Single: scalarized function	[44]
	NSGA-II: automated, flexible, and robust, these are tailored to solve multi-objective problems and return Pareto fronts, but do not provide a single optimum.	High	10+	Multiple: cost functions	[42,43,45,47]
Topology optimizations	Either *bidimensional* or *tridimensional*, they support automated optimum identification, are highly flexible, and promote substantial performance enhancements, but are limited to small design spaces, unless replicated unit-cell are used, and present challenges with accurate interface and multi-flow handling.	High to very high	1000+	Single: physical property or ratio	2D: [48–51] 3D: [52,53]

studies, such as those by Arie et al. [45] and Das et al. [47], explicitly integrate these practical constraints into the optimization process. This paper aims to address these gaps by developing an optimization strategy that explicitly targets end-user performance requirements rather than maximizing isolated component-level metrics. Unlike most existing approaches, which primarily focus on indicators such as the maximization of the j/f ratio, the proposed methodology is formulated around application-driven objectives, including the achievement of prescribed heat transfer rates and the compliance with allowable pressure-drop constraints. Moreover, the study also addresses the limited literature on optimization frameworks incorporating component-envelope redesign, by introducing a numerical framework capable of simultaneously adjusting internal features, such as channels and fins, and the overall heat exchanger dimensions and proportions. This integrated approach is essential to fully exploit the available optimization potential, as global heat exchanger geometry directly influences mass flow distribution and local channel velocities, which in turn govern internal feature performance. By jointly optimizing external and internal characteristics, the proposed framework captures these interactions and overcomes the limitations of sequential approaches, where internal and external geometries are optimized independently.

Accurate prediction of pressure losses in additively manufactured heat exchangers also remains a major modelling challenge. To address this issue, the present work extends previous developments on the thermal, hydraulic, and gravimetric modelling of AM heat exchangers for Selective Laser Melting (SLM), by integrating the validated algorithm of Ref. [54] into the proposed optimization framework, according to the scheme reported in Fig. 1.

1.1. Case study

Aiming to address the ever-growing need for enhanced fuel cell cooling in transport systems, the proposed methodology is applied to the refinement of three reference use cases:

- **Automotive.** A fully electric L3 H3 class van, powered by a 100 kW PEM fuel cell and comparable to the Mercedes e-sprinter [55] commercial vehicle. A fully loaded mass of 3000 kg is considered, along with an aerodynamic drag coefficient of 0.38, and a frontal area of about 5 m^2.
- **Aerospace.** A fully electric general aviation aircraft, inspired by the Cessna 172 Skyhawk [56], and powered by a 100 kW PEM fuel cell. A total mass of 1300 kg is assumed, with an approximate wing surface area of 18 m^2, and a NACA 2412 wing airfoil for preliminary estimation of the aircraft's lift and drag coefficients via the Airfoiltools database [57].
- **Marine.** A large scale sea transport vessel, with a total propulsive power of tens of MW and a maximum cruising speed of 14 kn [58,59]. In this case, a 100 kW HE represents a single cooling unit out of a much larger collection of heat dissipation modules collectively contributing to the total ship cooling demand.

A finned-microchannel HE with a nominal heat dissipation of 100 kW is considered for each case study, assuming pure water as the hot coolant and external dry air as the cold fluid.

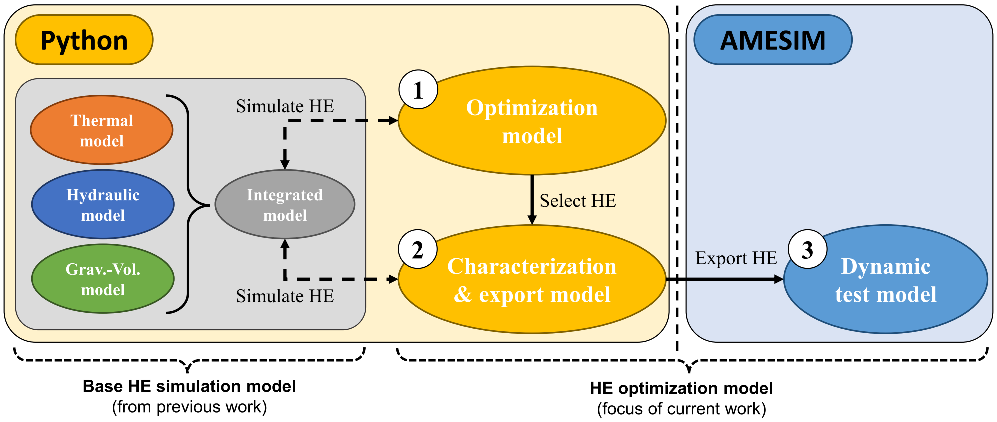

Fig. 1. Integration of previous thermo-hydraulic-gravimetric model from Ref. [54] with the proposed genetic optimization loop and full component characterization and export to a dedicated dynamic simulation model.

2. Methodology - Simulation model

The numerical model developed by the authors in Ref. [54] serves here as the core simulation element for the optimization framework. Based on a lumped-parameter formulation, it enables the rapid steady-state prediction of the thermal, hydraulic, volumetric, and gravimetric performance in compact cross-flow heat exchangers. The following sections detail the individual modelling approaches implemented within the framework.

2.1. Thermal model

The thermal behaviour of the HE is modelled according to the methodology presented by Mudawar et al. [25,60], based on the following assumptions:

- Steady-state regime;
- Uniform flow distribution;
- Uniform global heat transfer coefficient U;
- Uniform and constant fluid properties (assumed as the mean value between average inlet and outlet properties);
- Negligible heat loss from the plate's control volume;
- Negligible axial conduction;
- Adiabatic fin tips, with the channel walls acting as fins and the channel centreline representing the fin tips.

The heat exchanger is discretized into a series of geometrically and thermally identical plate modules, solving the three-dimensional component through a simplified two-dimensional representation, as illustrated in Fig. 2. The resulting formulation provides a computationally efficient representation while retaining the underlying heat transfer physics. Moreover, its modular structure facilitates extension to different heat exchanger geometries, as demonstrated by Northcutt and Mudawar [25], who applied the same methodology to both rectangular and annular aerospace heat exchanger configurations.

A dimensionless parameter, ϕ, is introduced following the mathematical derivation presented by Nacke et al. [60]. It represents the ratio between the mean fluid temperature difference and the inlet fluid temperature difference, as defined by Eq. (2):

$$\phi = \frac{1}{ab}\sum_{n=0}^{\infty}\left[1 - e^{-a}\sum_{k=0}^{n}\frac{a^k}{k!}\right]\left[1 - e^{-b}\sum_{k=0}^{n}\frac{b^k}{k!}\right] \tag{2}$$

where a and b are defined according to Eq. (3), with $\dot{m}_{h,plt}$ and $\dot{m}_{c,plt}$ expressing the fluid mass flow rates across a single plate, and $c_{p,h}$ and $c_{p,c}$ their corresponding specific heats.

$$\begin{cases} a = \dfrac{U\,W_{plt}\,L_{plt}}{\dot{m}_{h,plt}\,c_{p,h}} \\ b = \dfrac{U\,W_{plt}\,L_{plt}}{\dot{m}_{c,plt}\,c_{p,c}} \end{cases} \tag{3}$$

Eq. (4) [60] then returns the average heat transfer rate and outlet fluid temperatures of a single plate:

$$\begin{cases} q_{plt} = U\,W_{plt}\,L_{plt}[T_h(0,0) - T_c(0,0)]\phi \\ \overline{T}_{plt,h,out} = T_h(0,0) - a\,[T_h(0,0) - T_c(0,0)]\,\phi \\ \overline{T}_{plt,c,out} = T_c(0,0) + b\,[T_h(0,0) - T_c(0,0)]\,\phi \end{cases} \tag{4}$$

These can then be extended to the whole HE component following Eq. (5):

$$\begin{cases} q_{HE} = q_{plt}\cdot n_{plt} \\ \overline{T}_{HE,out} = \dfrac{\overline{T}_{plt,out}\cdot n_{plt} + \overline{T}_{0,0}(n_{layers} - n_{plt})}{n_{layers}} \end{cases} \tag{5}$$

where n_{plt} is the number of plates defined as $n_{plt} = \min(n_{h,layers}, n_{c,layers})$, assuming each layer as a row of adjacent channels containing the same fluid [54].

Eq. (6) models the thermal resistance scheme of the reference plate-module presented in Fig. 2:

$$\left(U\,W_{plt}\,L_{plt}\right)^{-1} = \frac{R_{conv,h} + R_{cond,w} + R_{conv,c}}{2} \tag{6}$$

where the conductive term $R_{cond,w}$ is determined through Eq. (7):

$$R_{cond,w} = \frac{H_w}{k\,W_{plt}\,L_{plt}} \tag{7}$$

assuming H_w as the wall thickness separating the two fluids, and k as the thermal conductivity of the heat exchanger structure. The convective terms of the hot and cold fluid are instead defined through Eq. (8), under the adiabatic fin tip hypothesis:

$$R_{conv} = \frac{1}{N_{fin}(\eta_{fin}\overline{h}_{fin}A_{fin} + \overline{h}_{base}A_{base})} \tag{8}$$

where N_{fin} is the number of fins per each plate of a given fluid, and $\overline{h}_{fin}$ and A_{fin} are its respective single half-fin heat transfer coefficient and wet area. $\overline{h}_{base}$ and A_{base} represent, instead, the heat transfer coefficient, and wet area of the channel surface between two consecutive fins, while η_{fin} is the channel fin efficiency, defined according to Eq. (9):

$$\eta_{fin} = \frac{\tanh\left(m_{fin}\frac{H_{fin}}{2}\right)}{m_{fin}\frac{H_{fin}}{2}} \qquad \text{with} \;\; m_{fin} = \sqrt{\frac{\overline{h}_{fin}P_{fin_{cs}}}{kA_{fin_{cs}}}} \tag{9}$$

where $H_{fin}/2$ is half the height of a channel fin, and $A_{fin_{cs}} = W_{fin}\cdot L_{fin}$ and $P_{fin_{cs}} = 2(W_{fin} + L_{fin})$ are the associated fin cross-section area and perimeter.

Following the approach from Ref. [61], the thermal resistance of a circular duct can also be solved through Eq. (9) by assuming an equivalent square geometry circumscribing the channels, with $D_{chan} = B_{chan} = H_{chan}$.

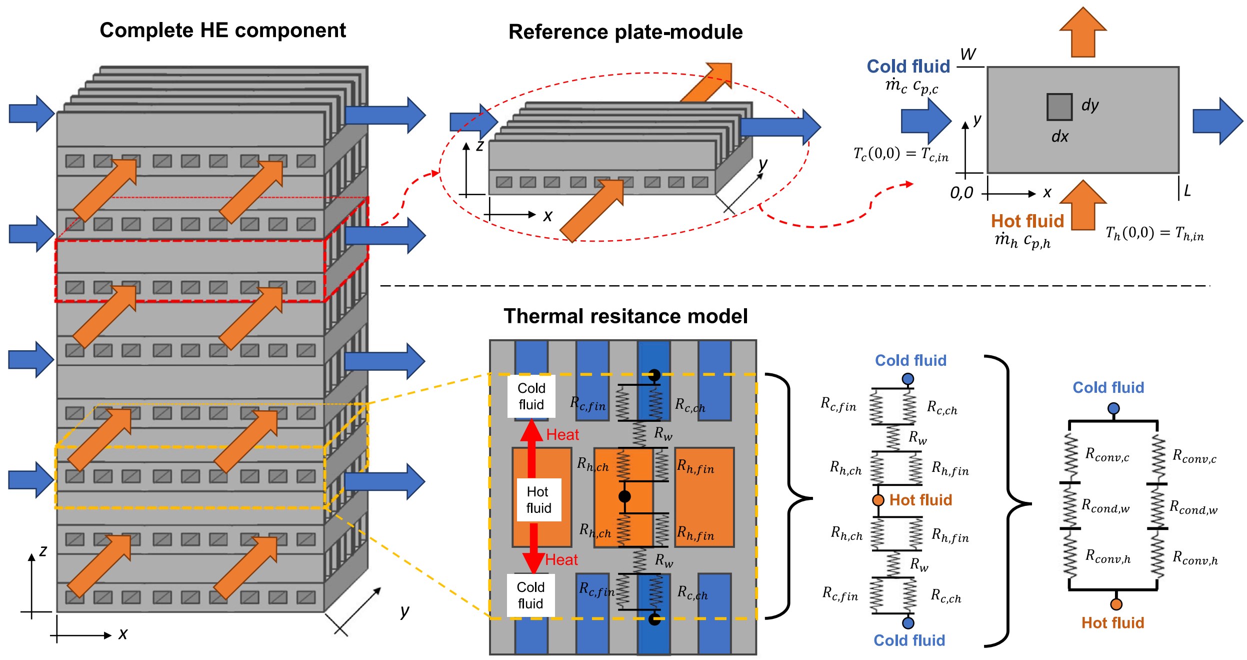

Fig. 2. Thermal model scheme showing: the complete heat exchanger (not to scale); a detail of the reference plate-module with its coordinate system; and the thermal resistance model associated with the plate. The resistance scheme is depicted with both fluid cross-sections oriented perpendicular to the viewer to simplify visualization; in practice, one row of cross-sections would be parallel to the viewer.

Table 2
Convective heat exchange coefficients of fluids.

Hypothesis	Regime	Equation
Finned-plate hypothesis: $\delta_{bl} < H_{chan}/2$ $\delta_{bl} < B_{chan}/2$ Assumes $Re = \frac{\rho u L_{chan}}{\mu}$, $Pr = \frac{c_p \mu}{k}$	Laminar, $Re < Re_{crit}$	$\frac{\bar{h} L_{chan}}{k} = 0.664\, Re^{1/2} Pr^{1/3}$ [63]
	Turbulent, $Re \geq Re_{crit}$	$\frac{\bar{h} L_{chan}}{k} = \left[0.664\, Re_{crit}^{1/2} + 0.037\left(Re^{4/5} - Re_{crit}^{4/5}\right)\right] Pr^{1/3}$ [63]
Closed-channel hypothesis: $\delta_{bl} \geq H_{chan}/2$ $\delta_{bl} \geq B_{chan}/2$ Assumes $Re = \frac{\rho u D_{hyd}}{\mu}$, $Pr = \frac{c_p \mu}{k}$, $D_{hyd} = \frac{4 A_{chan}}{P_{chan}}$	Laminar, $Re < 1800$	$\frac{\bar{h} D_{hyd}}{k} = \left[4.364^3 + 0.6^3 + a_{Nu}^3 + b_{Nu}^3\right]^{1/3}$, $a_{Nu} = 1.953 \sqrt[3]{Pr\, Re\left(\frac{D_{hyd}}{L_{hyd}}\right)}$, $b_{Nu} = 0.924 \sqrt[3]{Pr} \sqrt{Re\left(\frac{D_{hyd}}{L_{hyd}}\right)}$ [64,65]
	Transitional, $1800 \leq Re < 4000$	$\frac{\bar{h} D_{hyd}}{k} = \left(Nu_{lam}^6 + Nu_{turb}^6\right)^{1/6}$, $Nu_{lam} = 4.364 + \frac{0.086(1/l_{th})^{1.33}}{1+0.1\, Pr\left(Re D_{hyd}/L_{chan}\right)^{0.83}}$, $Nu_{turb} = \frac{(f/8)(Re-1000)Pr}{1+12.7(f/8)^{1/2}(Pr^{2/3}-1)}\left(1 + \left(\frac{L_{hyd}}{D_{hyd}}\right)^{-2/3}\right)$, $f = \frac{1}{4}\,(1.8 \log Re - 1.5)^{-2}$, $l_{th} = \frac{L_{chan}/D_{hyd}}{Re Pr}$ [66]
	Turbulent, $Re \geq 4000$	$\frac{\bar{h} D_{hyd}}{k} = \frac{(f/8)(Re-1000)Pr}{1+12.7(f/8)^{1/2}(Pr^{2/3}-1)}\left(1 + \left(\frac{L_{hyd}}{D_{hyd}}\right)^{-2/3}\right)$, $f = \frac{1}{4}\,(1.8 \log Re - 1.5)^{-2}$ [63,65,67]

Table 2 returns the empirical formulations for the convective heat transfer coefficients of both fluids, provided the maximum boundary layer thickness definition from Eq. (10) [62]:

$$\begin{cases} \delta_{bl} \simeq 5\, x\, Re_x^{-1/2} & \text{if} \quad Re_x < 5 \cdot 10^5 \text{ (laminar)} \\ \delta_{bl} \simeq 0.37\, x\, Re_x^{-1/5} & \text{if} \quad Re_x > 5 \cdot 10^5 \text{ (turbulent)} \end{cases} \quad \text{with } x_h = W_{plt},\ x_c = L_{plt} \tag{10}$$

Open-duct correlations are incorporated to enhance the flexibility of the numerical framework and ensure applicability across a wide range of explorable HE geometries during optimization. In particular, they provide a more appropriate representation of extreme configurations with few high-aspect-ratio channels and short flow lengths, where fully developed internal-flow assumptions may not be valid due to the boundary-layer height being smaller than half the distance to the opposite channel wall, preventing boundary-layer merging [60].

2.2. Hydraulic model

The hydraulic performance of a compact HE is modelled following the approach presented by Da Silva et al. [61], assuming idealized plenum-type headers at the heat exchanger interfaces. The pressure drop of both fluid streams is thus calculated according to Eq. (11) [68]:

$$\Delta p_{14} = \frac{G^2}{2\rho_2}\left[\left(1-\sigma^2\right) + K_{contr} + 2\left(\frac{\rho_2}{\rho_3} - 1\right) + \left(f_D \frac{L_{chan}}{D_{hyd}} \rho_2 \overline{\left(\frac{1}{\rho}\right)}\right)\right.$$

$$-\frac{\rho_2}{\rho_3}\left(1-\sigma^2\right)+\frac{\rho_2}{\rho_3}K_{exp}\Bigg] \tag{11}$$

assuming the following hypotheses, along with the previous ones:

- Uniform velocity profile;
- Constant fluid properties;
- Incompressible fluid flow, for Mach numbers lower than 0.3 [69]. Assuming air as the only compressible fluid of reference in this work, this hypothesis is valid as long as the local gas speed does not exceed $100\,\mathrm{m\,s^{-1}}$.

The irreversibility factors K_{contr} and K_{exp} are tabulated and parametrized within the model based on the empirical diagrams reported by Kays and London [70], as functions of the fluid's Reynolds number and the porosity factor σ, defined as the ratio between the frontal area of the HE and the total cross-sectional area of all channels ($\sigma = \frac{A_2}{A_1} = \frac{A_3}{A_4} < 1$).

The Darcy friction factor f_D is, instead, calculated according to the Churchill's formulation of Eq. (12) [71]:

$$\begin{cases} \Phi_1 = \left[-2.457\ln\left(\left(\frac{7}{Re}\right)^{0.9}+0.27\frac{\epsilon}{D_{hyd}}\right)\right]^{16} \\ \Phi_2 = \left[\frac{37\,530}{Re}\right]^{16} \\ f_D = 8\left[\left(\frac{8}{Re}\right)^{12}+\left(\Phi_1+\Phi_2\right)^{-1.5}\right]^{\frac{1}{12}} \end{cases} \quad \text{with } Re = \frac{\rho u D_{hyd}}{\mu} \tag{12}$$

Following Ref. [54], Ra/D_{hyd} is used as a first-order estimate of ϵ/D_{hyd} [61,72,73], as Ra remains the most widely adopted experimental measure of surface roughness due to its accessibility and widespread use. This choice is made while acknowledging that arithmetic mean roughness Ra does not directly represent the equivalent Colebrook sand–grain roughness ϵ, which itself does not correspond to a directly measurable physical feature, and that no universally agreed correlation between the two quantities exists.

A corrective factor $K_p = 1.3$ [54] is finally applied to account for pressure drop underestimation in AM heat exchangers at higher Reynolds number, following Eq. (13):

$$\Delta p_{14,corr} = K_p \Delta p_{14} \tag{13}$$

This factor is introduced as a pragmatic, first-order engineering correction to compensate for the systematic under-prediction of pressure losses when using conventional channel-loss formulations in additively manufactured geometries. While it does not fully capture the underlying physical mechanisms governing AM-induced pressure drop increases, it provides a conservative correction within the reduced-order modelling framework adopted in this study, prioritizing computational efficiency over detailed hydraulic fidelity. Studies such as Kercher et al. [74] highlight the strong influence of geometry-induced flow disruption in ribbed-fin configurations, further supporting the general observation that pressure loss deviations from smooth-channel behaviour can be significant, although such correlations are not directly transferable to AM roughness-driven flows. Nevertheless, the proposed simulation framework remains modular and well suited to accommodate higher-fidelity hydraulic models, and future developments may incorporate experimentally derived AM roughness characterizations and more advanced pressure-loss models, as discussed in recent reviews such as Thole et al. [75].

2.3. Volumes and masses model

The volumetric footprint of a compact HE is determined through Eq. (14). A rectangular cuboid approximates the space occupied by the component, while the channels are assumed as straight ducts. The metallic structure enveloping the fluids is derived as the boolean difference between the total HE volume, and the combined channels volumes, as given in Eq. (15).

$$\begin{cases} V_{HE} = L_{HE}\cdot W_{HE}\cdot H_{HE} \\ V_h = \left(n_{h,layers}\cdot n_{h,fin}\right)\cdot A_{h,chan,cs}\cdot W_{HE} \\ V_c = \left(n_{c,layers}\cdot n_{c,fin}\right)\cdot A_{c,chan,cs}\cdot L_{HE} \end{cases} \tag{14}$$

$$V_s = V_{HE} - V_h - V_c \tag{15}$$

Multiplying each volume V by the corresponding material density ρ provides the mass of each component. These contributions are then combined according to Eq. (16) to obtain the total heat exchanger mass and its gravimetric performance.

$$m_{HE} = V_h\cdot\rho_h + V_c\cdot\rho_c + V_s\cdot\rho_s \tag{16}$$

2.4. Integrated numerical model

Ultimately, a single integrated algorithm combines and orchestrates the execution of the previously presented thermal (Section 2.1), hydraulic (Section 2.2), volumetric, and gravimetric (Section 2.3) models, following the approach from Ref. [54]. This integrated script iteratively computes and refines the main simulation unknowns, represented by the fluids outlet temperatures and inlet pressures. Starting with an initial hypothesis of negligible heat transfer and pressure drops, the model derives the corresponding fluid properties at the HE outlet and inlet sections, using the python CoolProp library from Bell et al. [76]. These properties then drive heat transfer and pressure drop determination according to the methods from Sections 2.1 and 2.2. The resulting outlet temperatures and inlet pressures are then used to refine the fluid properties at each section, iterating the process until the computed parameters converge with those assumed to extract fluid properties.

This approach closely matches the methodology presented in the textbook by Nellis and Klein [77] when it models the discretized temperature distribution of working fluids in cross-flow HEs. Notably, in the authors' formulation, the initial guess for the outlet fluid temperatures is set as the average between the hot and cold streams inlet temperatures rather than their respective entrance values. This strategy promotes a faster numerical convergence of the model, but is not directly applicable when modelling pressure drops, as the pressure field on each side evolves independently of the hydraulic losses on the opposite fluid. Hence the negligible pressure drop hypothesis was considered for this study, as per Ref. [54], while a negligible heat-transfer assumption was also introduced for numerical consistency.

This complete loop enables a comprehensive characterization of the component's behaviour, provided only the fluids mass flow rates, their inlet temperatures, and outlet pressures, along with the key design geometry parameters. The relevant outputs of the simulation are: the heat transfer of a single plate, the total heat transfer of the complete HE, the pressure drops of both fluids, their respective outlet temperatures and inlet pressures, the masses and the volumes of the enclosed fluids and HE structure.

3. Methodology - Design optimization

A dedicated design optimization framework calls the reference HE characterization model to evaluate the performance of candidate solutions, iteratively refining their geometric parameters to maximize the selected performance objectives. Following the work of Arie et al. [45], a GA is adopted for this purpose due to its robustness and suitability for multi-objective optimization problems involving numerous design variables. Although GAs generally converge more slowly than alternative methods, such as gradient descent, the low computational cost of the core HE characterization model offsets this limitation, enabling robust exploration of large and complex design spaces with a modest computational cost.

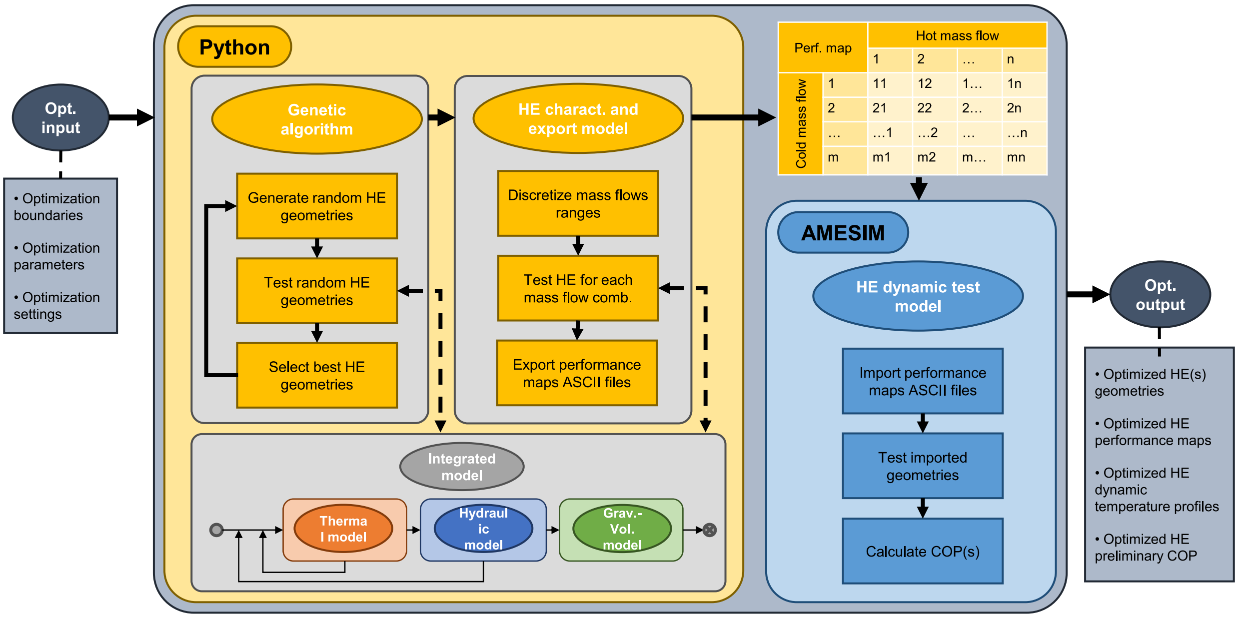

Fig. 3. Functional scheme of the proposed HE design optimization loop. The representation details the main steps of the process, highlighting the interfaces between the various sub-models and simulation environments.

The resulting non-dominated solution(s) are subsequently subjected to a comprehensive performance characterization over a range of flow conditions, enabling the export of optimized geometries to other simulation environments. Finally, a dynamic simulation model is also developed in AMESim to evaluate the exported solutions under realistic, time-dependent heat load profiles.

Fig. 3 illustrates this workflow, as detailed in the following sections.

3.1. Genetic optimization model

The Python library PyGAD [78] implements the evolutionary algorithm framework and manages its execution. The tool first generates an initial population of random solutions (chromosomes). Then, it iteratively recalls the modelling script described in Section 2 to evaluate the predicted performance of each chromosome, returning the output parameters used to derive the cost functions.

Four different types of parameters define the essential inputs of the optimization: the optimization genes, the optimization boundaries, the optimization targets, and the optimization settings.

3.1.1. Optimization genes

Each chromosome is characterized by a set number of genes, with every gene representing a key geometrical parameter influencing the performance of the final design. For the present study, which aims to optimize an additively manufactured compact HE featuring circular or rectangular ducts, 10 variables are sufficient to fully describe the component geometry, as shown in Fig. 4. The admissible range assigned to each gene defines the design space explored by the optimization algorithm, with each chromosome representing a unique candidate HE geometry.

A design space of $1000 \times 1000 \times 1000\ \mathrm{mm}^3$ is considered for this study, aligning with typical lengths of commercially available 100 kW automotive radiators [79,80], and the smaller general aviation cabin widths [56]. Arbitrary minimum values of 25 mm are then assumed to avoid instances of null design space dimensions.

The expected laser melting pool dictates the minimum size of the internal features for an AM component. Assuming a LSM pool diameter of 160 μm, comparable to those of Kempen [81], Minetola et al. [82], and da Silva et al. [61], a minimum fin and wall thickness of 0.16 mm is established. A minimum channel width and height of 0.84 mm is assumed,

Table 3
GA chromosomes' genes.

Gene name	Symbol	Optimization range [mm]
Main dimensions		
HE height	H_{HE}	25 mm–1000 mm
HE length	L_{HE}	25 mm–1000 mm
HE depth	W_{HE}	25 mm–1000 mm
Internal dimensions		
Separating wall thickness	H_w	0.16 mm–10 mm
Hot side channel height	$H_{chan,h}$	0.84 mm–1000 mm
Hot side channel width	$B_{chan,h}$	0.84 mm–1000 mm
Hot side fin width	$B_{fin,h}$	0.16 mm–10 mm
Cold side channel height	$H_{chan,c}$	0.84 mm–1000 mm
Cold side channel width	$B_{chan,c}$	0.84 mm–1000 mm
Cold side fin width	$B_{fin,c}$	0.16 mm–10 mm

considering a minimum design shape of 1 mm × 1 mm, shrunken by the melting pool diameter of 160 μm. An upper fin thickness boundary of 10 mm is considered, while the channels' maximum height and width values are set to match their corresponding HE maximum dimension of 1000 mm.

Table 3 collects all the genes assumed this study and their respective value ranges.

However, validation checks are applied once the genes are translated into the corresponding geometrical parameters for performance evaluation within the core simulation model. These checks prevent the generation of unfeasible or inconsistent geometries, such as channel base lengths exceeding the corresponding HE dimensions or channel row arrangements protruding beyond the available base plate length. Similarly, these checks also ensure that the individual plate heights and the cumulative stacked plate height remain within the limits imposed by the main HE height parameter. Further details on the validation logic and governing equations are provided in Appendix.

3.1.2. Optimization boundaries

The optimization boundaries define a set of predefined physical parameters that remain constant throughout the entire optimization process across all chromosomes and generations. These include the fluid mass flow rates, inlet temperatures, and outlet pressures, which

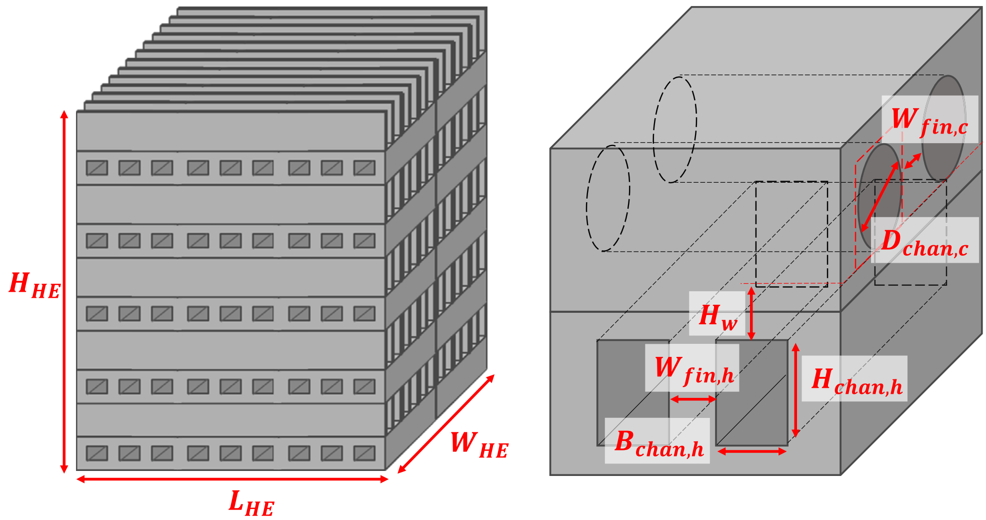

Fig. 4. Representation and nomenclature of every chromosome gene employed for the evolutionary design optimization of the HE. A combined circular-rectangular channel configuration is provided, on the left, to evidence differences between optimization parameters of the two shapes.

are set to be representative of a relevant operating condition of the heat exchanger, against which the design is optimized.

For the purpose of this study, pure water is assumed as the hot fluid, while dry air represents the cold fluid of the HE. These assumptions simplify the characterization of the optimization problem while remaining consistent with the working fluids adopted for the validation of the integrated simulation model [54,61]. The adoption of pure water as the reference coolant, instead of more conventional water–glycol mixtures employed in thermal management systems, represents a first-order approximation of the cooling conditions, yet provides a physically meaningful baseline, as deionized water can be employed when reduced electrical conductivity and insulation requirements are relevant. More advanced working fluids, including water–glycol mixtures, humid air, vapour, and alternative coolant formulations, are left for future investigations.

An inlet water-coolant temperature of 70 °C is assumed, roughly equivalent to the typical limit operating temperature of PEM fuel cells [16]. Conversely, an air inlet temperature of 40 °C is selected to represent a typical hot-day condition, corresponding to a common worst-case scenario (WCS) for both automotive [83] and aerospace [84] cooling. The analysis considers an HE outlet pressure of 1.013 25 bar for both fluids, while a maximum volumetric mass flow of 200 L min^{-1} is assumed for the coolant, approximately equivalent to 3.3 kg s^{-1} of pure water mass flow. Conversely, the air mass flow rate is modelled as a function of the air velocity impinging the cold-side frontal area of the HE, according to Eq. (17):

$$\dot{m}_{air} = \left(H_{HE} \cdot W_{HE}\right) u_{air}\, \rho_{air} \tag{17}$$

where H_{HE} and $W_{HE,h}$ are the airside HE height and width, defining its frontal area; u_{air} is the airspeed impinging on the device; and ρ_{air} is the free-stream air density, assumed equal to 1.127 kg m^{-3} at 40 °C and sea-level conditions.

For simplicity, the airspeed u_{air} is assumed to approximately match the instantaneous vehicle speed. Accordingly, the following airspeeds are considered for the optimization of each application:

- **Automotive**: 36 m s^{-1}, consistent with the nominal maximum speed of a van travelling at 130 km h^{-1} on a highway.
- **Aerospace**: 36 m s^{-1}, representative of a typical general aviation take-off speed of approximately 130 km h^{-1} and selected by considering the late take-off phase as the most critical operating condition, as identified by Asli et al. [84]. This condition is consistent with the previously defined ground-level air density and temperature assumptions for the design optimization.
- **Marine**: 7.2 m s^{-1} for a slow moving, large scale vessel with a maximum cruising speed of 14 kn. However, assuming the presence of a fan/compressor unit ensuring a minimum airspeed supply of 10 m s^{-1}, this latter value is adopted as the reference u_{air} instead.

Table 4
GA optimization boundaries and targets.

Boundary name	Symbol	Value
Integrated HE model inputs		
Hot fluid inlet temperature	$T_h(0,0)$	70 °C
Hot fluid outlet pressure	$p_{4,h}$	1.013 25 bar
Hot fluid mass flow	$\dot{m}_h$	3.3 kg s^{-1}
Cold fluid inlet temperature	$T_c(0,0)$	40 °C
Cold fluid outlet pressure	$p_{4,c}$	1.013 25 bar
Cold fluid mass flow	$\dot{m}_c$	Automotive/Aerospace: $40.57\left(H_{HE} \cdot W_{HE}\right)$ Marine: $11.27\left(H_{HE} \cdot W_{HE}\right)$
Optimization targets		
HE heat transfer	$\dot{q}_{HE}^{target}$	100 kW
Maximum hot fluid pressure drop	$\Delta p_{14,h}^{target}$	50 kPa
Maximum cold fluid pressure drop	$\Delta p_{14,c}^{target}$	50 kPa

Table 4 summarizes all optimization boundaries and their associated values.

3.1.3. Objective functions

Objective functions define the optimization goals by processing the outputs of the numerical model from Section 2.4 to evaluate and rank each chromosome, enabling the identification of the best-performing solutions. Within PyGAD [78], these functions are referred to as “fitness functions”, which the algorithm maximizes to progressively refine the solution(s). Accordingly, Eq. (18) details a fitness function targeting HE mass minimization, while Eq. (19) supports the maximization of the component’s thermal effectiveness:

$$f'_{mass} = k_{f,mass}/m_{HE} \tag{18}$$

$$f'_{eff} = \varepsilon_{HE} \tag{19}$$

A corrective factor k_{mass} normalizes the content of Eq. (18) by the minimum expected component mass, improving results readability and enabling comparison between the two functions' outcomes.

A corresponding heat transfer maximization equation can also be defined according to Eq. (20):

$$f'_{heat} = q_{HE}/k_{f,heat} \tag{20}$$

A set of additional corrective factors discourages the selection of solutions failing to meet heat transfer and pressure drop requirements. Eq. (21) penalizes the fitness values of any chromosome deviating from the heat dissipation target (100 kW) by more than 1 kW:

$$\text{If } \left|\dot{q}_{HE} - \dot{q}_{HE}^{target}\right| > 1 \text{ kW} \qquad \Rightarrow f'' = \frac{f'}{\left(\dot{q}_{HE} - \dot{q}_{HE}^{target}\right)^2} \tag{21}$$

This 1 kW tolerance prevents excessively large penalties near the target value, while division by the squared error increases the penalization of solutions far from the target and ensures a strictly positive denominator.

Eq. (22), instead, penalizes any solution exceeding preset pressure drop thresholds of $\Delta p_{14,h}^{\text{target}}$ and $\Delta p_{14,c}^{\text{target}}$, by reducing their fitness values proportionally to the square of the corresponding pressure ratio. For the purpose of this study, a maximum tolerable hydraulic loss of 0.5 bar is considered for both the coolant and air streams:

$$f''' = f'' \cdot \left[\min\left(1, \left(\frac{\Delta p_{14,h}^{\text{target}}}{\Delta p_{14,h}}\right)^2\right) \cdot \min\left(1, \left(\frac{\Delta p_{14,c}^{\text{target}}}{\Delta p_{14,c}}\right)^2\right)\right] \tag{22}$$

Table 4 summarizes the assumed optimization boundaries and target constraints from Eqs. (21) and (22).

Additional constraints may be introduced following the same penalty-based rationale. For instance, marine applications could incorporate environmental and operational constraints, such as enforcing a maximum allowable seawater discharge temperature. However, since the objective of the present work is to develop and demonstrate a component-level heat exchanger optimization methodology and to assess its applicability across three different application domains, such application-specific considerations remain beyond the scope of this study and are left to future dedicated investigations.

3.1.4. Optimization settings

The optimization settings define the GA hyper-parameters, including the total number of generations, the number of chromosomes per generation, and the number of genes per chromosome. A Non-dominated Sorting Genetic Algorithm II (NSGA-II) is adopted from the PyGAD library [78] as the parent selection method to simultaneously handle multiple fitness functions and enable multi-objective optimization. Finally, the elitism rate, mating selection rate, mutation rate, and mutation type influence the effectiveness and speed at which new non-dominated solutions are discovered. With the exception of the number of genes and the parent selection method, the remaining hyper-parameters are progressively refined to enhance the algorithmic efficiency and convergence, resulting in the values reported in Table 5.

The presented optimization approach is applied here to refine a selection of HE layouts for three reference applications: automotive, aerospace, and marine, in compliance with constraints from Tables 3 and 4. AISI 316 stainless steel is considered for the HE structure instead of more conventional Al-based alloys, as it is an iron-based material compatible with both AM and conventional fabrication processes, consistent with earlier studies used for the validation of the reference HE simulation model [54,61]. The material has an average density of 8000 kg m^{-3} and a thermal conductivity of approximately 15 W m^{-1} K^{-1}. Focusing on the optimization of a compact HE design for AM, a channel surface roughness Ra of 12.21 μm is also considered, consistent with experimental measurements from da Silva et al. [61].

Table 5
GA optimization hyper-parameters.

Setting	Value
Number of generations	2000
Number of chromosomes	500
Number of genes	10
Elitism rate	5%
Selection rate (mating chromosomes)	60%
Selection method	NSGA-II
Crossover type	Uniform
Mutation rate	5%
Mutation type	Random resetting

3.2. Export model

A dedicated export model computes and saves the relevant data about the non-dominated solutions identified by the GA for use in other software and simulation tools. It does so by performing a comprehensive characterization of the design's performance, simulating its behaviour outside the optimization boundary conditions, and collecting the data into structured performance maps for export.

The integrated HE model from Section 2.4 is recalled to characterize the behaviour of the selected design(s) across feasible combinations of thermal fluid flow rates. These combinations are collected within a discretized flow-rate matrix, over which the integrated model evaluates the heat transfer performance and pressure drops of each selected design. Eqs. (23) and (24) process these outputs, generating a thermal effectiveness matrix and two hydraulic-loss factor ζ vectors:

$$\begin{aligned}\varepsilon_{HE}\left(\dot{m}_h, \dot{m}_c\right) &= \frac{\left|\dot{q}_{HE}\right|}{\left|C_{min}\left(T_h(0,0) - T_c(0,0)\right)\right|} \qquad \text{with } C_{min} \\ &= \min\left(\overline{c_p}_h \dot{m}_h, \overline{c_p}_c \dot{m}_c\right)\end{aligned} \tag{23}$$

$$\zeta(Re) = \frac{2\overline{\rho}\left(A_2\right)^2 \Delta p_{14}}{\dot{m}^2} \tag{24}$$

The resulting $\varepsilon_{HE} = f\left(\dot{m}_h, \dot{m}_c\right)$ matrix and $\zeta = f(Re)$ vectors are respectively structured according to the AMESim 2-D and 1-D standard table formats and exported into 3 dedicated ASCII files. Additionally, 12 complementary simulation parameters, arranged in the AMESim "global parameters" string format, complete the characterization export. These include:

- The Hydraulic diameters of both fluids' channels (2 parameters)
- The combined cross-sectional area of all channels for each fluid (2 parameters);
- The total volume occupied by each fluid (2 parameters);
- The dry mass of the HE (1 parameter);
- The directory paths and filenames of the generated ε and ζ ASCII tables (3 parameters);
- The mass flow rates assumed as optimization boundaries for the two fluids (2 parameters).

3.3. Dynamic model

A dynamic simulation model evaluates the performance of the optimized HE design(s) under variable heat load conditions, reproducing realistic operating scenarios. The model is developed in AMESim and consists of six main components and four sensorized sections, as illustrated in Fig. 5. Short pipe lengths of 0.1 m are assumed between each component to minimize the influence of connecting lines on the simulation results, together with relatively large channel diameters of 25 mm for the coolant and 500 mm for the air.

The HE component, located at the centre of Fig. 5, represents the main element of the virtual test bench, consisting of tree main

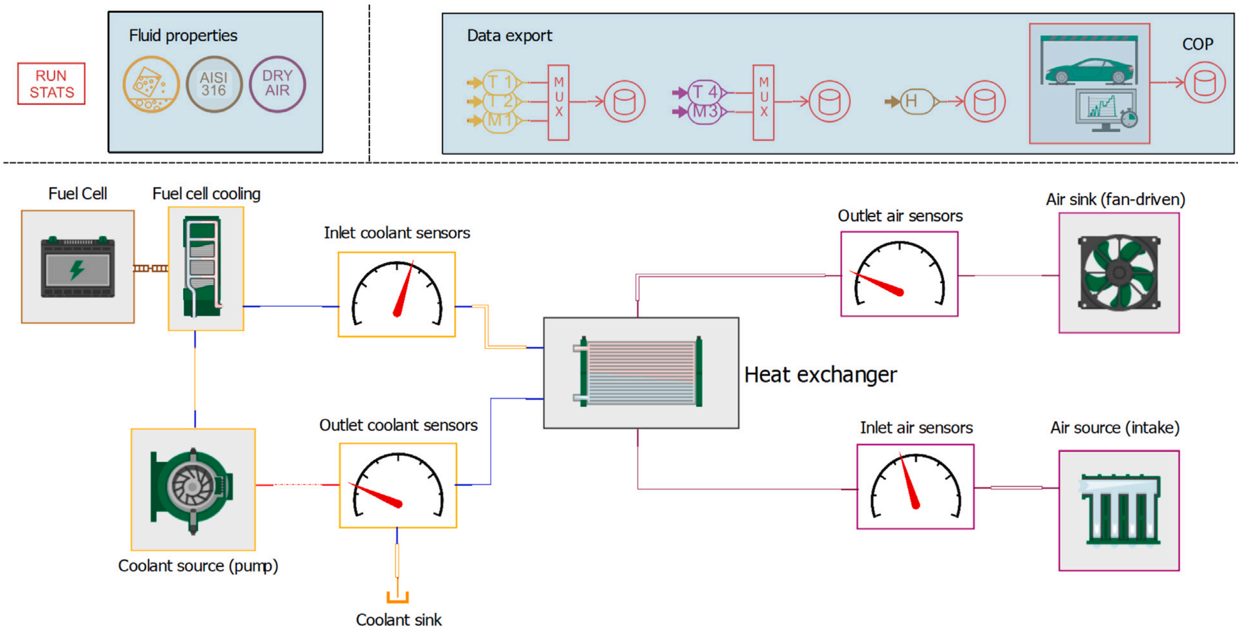

Fig. 5. AMESim model for the dynamic simulation of the HE performance.

subcomponents: the liquid coolant, the external air, and the dry HE structure. Fully characterized through the import of Python-generated performance maps and global parameters, it evaluates the heat transfer between the fluids and the associated pressure losses. The model drops the steady-state hypothesis, introducing the thermal capacitance of both fluid streams, defined from their occupied volumes and average densities, and the that of the dry HE structure, calculated from the component mass according to $C = c_p m$. Fluid and material properties are directly extracted by the software from the substances defined in the properties tab. Consistent with the previous GA settings, pure water is considered as the reference hot coolant, while dry air is adopted as the cold fluid.

A dynamic signal models the fuel cell's waste heat from the cooling system's perspective, applying the heat load profile to the coolant loop via the fuel cell cooling component. The coolant loop is modelled as an open circuit, allowing for the fluid's thermal expansion to discharge directly into the coolant sink, and eliminating the need for a dedicated expansion tank. However, to emulate continuity between the circuit inlet and outlet sections, the outlet temperature signal is fed back to the coolant source component, reproducing a closed-loop behaviour that is more representative of real-world applications.

A pneumatic circuit models the airflow. Comprising an intake source element and a fan-driven sink component, the air-loop is also implemented as an open system. However, in this case, no temperature feedback is introduced, as the air circuit is indeed open in real-world applications. In line with considerations from Section 3.1, the model calculates the air mass flows according to Eq. (17), given the local air density and the instantaneous vehicle airspeed saturated to a minimum of $10\,\mathrm{m\,s^{-1}}$.

Ultimately, four sensors collect data at the heat exchanger inlet and outlet sections, and route them to dedicated export blocks in the upper-right portion of Fig. 5, where they are saved for post-processing. Eventually, customizable Coefficients of Performance (CoPs) are also defined, tracking relevant figures of merit, and exporting them for future comparison with other designs.

3.3.1. Input dynamic profiles

Within the dynamic model, all optimization boundaries from Table 4 translate into time-variable simulation inputs. Values from Table 4 are preserved for the coolant loop mass flow $\dot{m}_h$ and outlet pressure $p_{4,h}$, here assumed as constants. The coolant inlet temperature $T_h(0,0)$, as anticipated, is instead addressed through the feedback loop described in Section 3.3.

Conversely, the air temperature and pressure are determined from the simulated transport system altitude using the International Standard Atmosphere (ISA) model [85], adjusted for a 40 °C ground hot-day scenario. For the automotive and marine applications, altitude variations are assumed negligible, whereas the aircraft case accounts for the non-negligible altitude changes associated with a reference flight profile. The instantaneous air mass flow rate is instead imported from input files generated according to the mission profiles described in the following section, along with the fuel cell heat load profiles.

For the automotive application, the Worldwide Harmonized Light Vehicle Test Procedure (WLTP) is chosen as the reference speed profile. Following the formulations from Gillespie [86], the vehicle's free-body diagram is modelled and solved in AMESim to compute the tractive force required to follow the selected speed profile, assuming null inclination and absence of hitched masses. The instantaneous tractive power at the wheel shaft is then computed multiplying the obtained tractive force by the speed profile, while the negative contributes, associated with car braking, are excluded through signal saturation.

For the aerospace use case, the EASA-FTP-01-00 test flight for ultra-light aircraft and general aviation [87] is adopted as the reference mission profile. The aircraft's free-body diagram is modelled in AMESim according to the formulations of Cook et al. [88], as simplified by the NASA Glenn Research Center in its introductory lectures on aircraft dynamics [89]. The model computes the thrust force required by the aircraft to complete the mission profile, and employs it to derive the required propulsive power at the propeller shaft, assuming an approximate propeller efficiency of 70%. Additionally, a minimum power saturation of 18 kW is considered for the descent phase.

For the marine scenario, the existing navigation data and models provided with the AMESim demonstration model for maritime fuel consumption prediction are adopted. The dataset simulates a two-and-a-half-day voyage of a large vessel travelling from Norway to France at a maximum calm-sea speed of 14 kn. Following appropriate modifications, the vessel shaft power demand is computed directly within the adapted model, accounting for the ship's geometry, speed, mass, and propeller efficiency inherited directly from the original DEMO specifications.

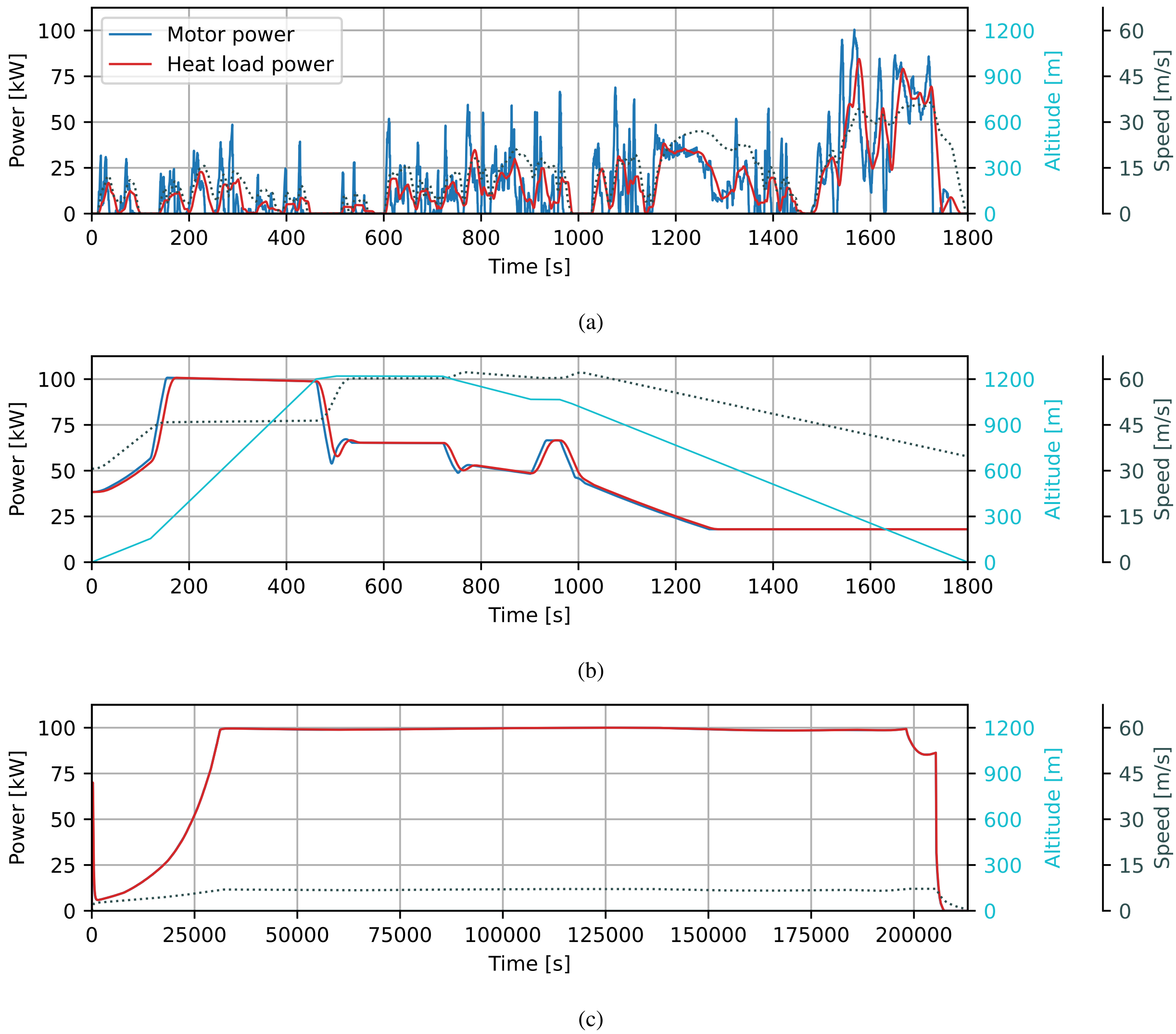

Fig. 6. Dynamic electric power request, and fuel cell waste heat generation profiles of all three reference applications: 6(a) L3 H3 van performing a WLTP drive cycle. 6(b) General aviation aircraft executing the EASA-FTP-01-00 reference flight test. 6(c) Large scale transport vessel completing a two and a half day voyage, based on predefined AMESim navigation data. Values of the marine application are normalized to 100 kW for consistency with the optimized HE design.

Given the shaft power requirements of each application, Eq. (25) returns the corresponding electrical power demand, assuming a driveline efficiency $\eta_{driveline}$ of 95%, and an electric motor efficiency $\eta_{e-motor}$ of 95% across all case studies:

$$P_{electric} = \frac{1}{\eta_{driveline}} \frac{1}{\eta_{e-motor}} P_{shaft} \tag{25}$$

The fuel cell system supplies the required propulsion power. However, owing to the inherently slow dynamics of fuel cells, an auxiliary battery is assumed to accommodate the high-frequency power fluctuations, while the fuel cells supply the average, low-frequency power demand. This power-splitting strategy is emulated by applying a moving-average filter with a reference time constant of 20 s to the electric motor power demand. The resulting smoothed power profile is then used to compute the fuel cell waste heat generation according to Eq. (26), assuming a nominal 50% fuel cell efficiency η_{FC}:

$$\dot{q}(t) = \frac{1}{T} \int_{t-T}^{t} \frac{1 - \eta_{FC}}{\eta_{FC}} P_{e-motor}(\tau)\, d\tau \qquad \text{with} \;\; T = 20\,\text{s} \tag{26}$$

The resulting heat load profile is then fed back to the dynamic simulation model as a thermal input to the fuel cell cooling component. However, for the large-scale marine application, this heat generation profile is first normalized to a maximum of 100 kW to match the scale of the optimized heat exchanger. This assumes that the total vessel heat rejection is distributed across multiple smaller heat dissipation units that collectively satisfy the ship's cooling demand. This simplification is adopted to preserve a consistent component-level scale and optimization framework across the three reference case studies, enabling a direct comparison of the proposed methodology across different application domains. Accordingly, application-specific and system-level aspects, including multi-unit arrangements, overall system layouts, multi-pass configurations, intake geometry effects, and other installation-dependent constraints, are intentionally excluded from the present formulation to maintain the general applicability of the proposed methodology and are more appropriately addressed in dedicated application-specific investigations.

Fig. 6 illustrates the electric power demand and corresponding fuel cell waste heat generation computed under these assumptions for each of the reference applications application.

4. Results

In the following sections, the results of the evolutionary optimization, performed according to the specifications reported in Tables 3

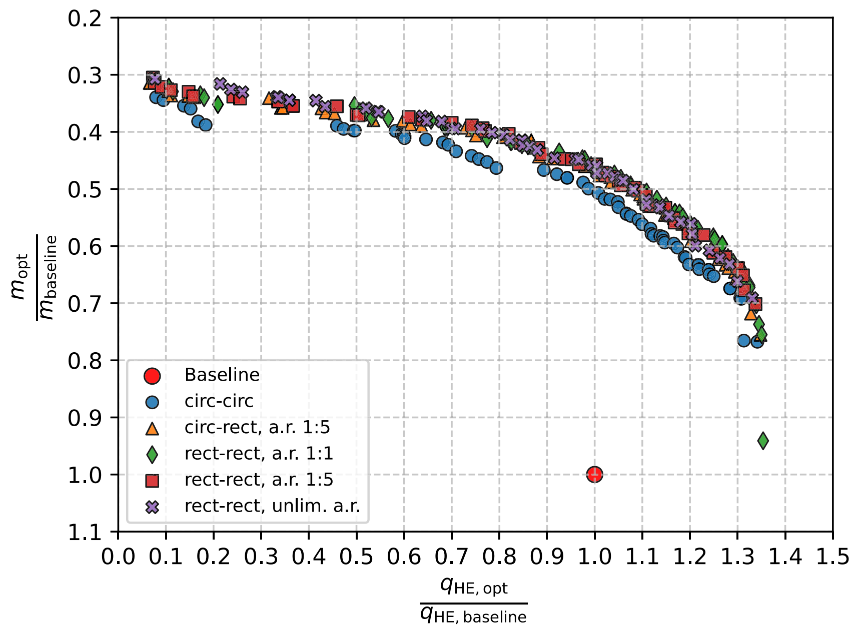

Fig. 7. Pareto frontiers for mass minimization and heat transfer rate maximization of the reference geometry of Ref. [61]. Comparison between five different channel shape configurations: circular–circular, circular–rectangular (1:5 max aspect ratio), square–square (1:1 max aspect ratio), rectangular–rectangular (1:5 max aspect ratio, both), and rectangular–rectangular (unrestricted max aspect ratio).

and 4, are first presented and subsequently assessed through dynamic simulation.

4.1. Optimization performance assessment

Before proceeding with the optimization of the three reference use cases, the optimization framework is first assessed against a literature case, evaluating optimized geometries within a design space constrained to the original dimensions of the experimental module from Ref. [61]. Accordingly, a 100 × 100 × 100 mm design domain is considered, encompassing the HE cross-channel core and the 25 mm flange couplings extending above and below the core, preserving the geometric proportions of the original configuration. The minimum design space genes dimensions are increased from 25 mm to 55 mm to accommodate these flanges, while the minimum internal feature sizes are retained from Table 3. The corresponding upper gene boundaries are consistently downscaled by a factor of 1/10 for the internal features to reflect the reduced design space.

The optimization problem is formulated to minimize component mass while maximizing heat transfer under the inlet conditions of the T60C5 experimental test from Ref. [61]. These correspond to a hot-water mass flow rate of $0.2665\,\mathrm{kg\,s^{-1}}$ at 60.2 °C, and a cold-air flow of $0.0272\,\mathrm{kg\,s^{-1}}$ at 23.8 °C, for which the baseline geometry achieves approximately 537 W of heat transfer. To allow broader performance exploration, the heat transfer constraint of Eq. (21) is relaxed for this analysis, whereas the pressure drop thresholds in Eq. (22) are reduced to 0.25 bar, in line with data from the reference experimental case.

The optimization is conducted for a population of 200 chromosomes and refined over 500 generations. Provided the high computational efficiency of the reference simulation model, the complete optimization is executed in approximately 20 min on a personal workstation with an AMD Ryzen 7 7800X3D processor and 32 GB of RAM using a single-core (serial) implementation. This decreases to less than 15 min when a parallelized approach utilizing 5 cores is employed. This computational cost is modest compared with higher-fidelity approaches, such as the topology optimization (TO) framework reported in Ref. [52], which required up to 8 days of computational effort using 30 processing units for the exploration of a comparable design space.

The resulting non-dominated solutions are analysed considering five representative internal channel geometries: the reference all-circular configuration; a mixed circular–rectangular configuration with rectangular cold-side channels limited to a maximum aspect ratio of 1:5; all-square channels (maximum aspect ratio of 1:1); rectangular channels constrained to a maximum aspect ratio of 1:5; and rectangular channels with unbounded aspect ratio. The corresponding Pareto-optimal frontiers are presented in Fig. 7, normalized with respect to the baseline geometry values to facilitate the quantification and comparison of performance gains. The results demonstrate the capability of the proposed methodology to identify improved HE designs with enhanced thermal–hydraulic performance. In particular, mass reductions of up to 50% can be achieved while preserving the nominal thermal behaviour of the baseline configuration. Alternatively, heat transfer can be increased by up to 31% while still enabling a 24% reduction in mass. Furthermore, the adoption of rectangular channel geometries consistently improves the optimization outcomes, providing an additional mass reduction of approximately 5% compared with circular configurations.

4.2. Genetic algorithm results

Having demonstrated the performance gains enabled by the proposed design optimization approach, the settings summarized in Table 5 are herein applied to the reference use cases of this study. The heat transfer optimization target is reintroduced, while the evolutionary algorithm is initialized with a randomly generated population, simultaneously targeting mass minimization and thermal effectiveness maximization via the fitness functions in Eqs. (18) and (19). Owing to the large design space defined in Table 3, an increased population size and number of generations are required to ensure comprehensive exploration, with a computational time of approximately 4 h for the evaluation of approximately 10^6 design configurations on a single-core (serial) implementation. Rectangular channels with a maximum aspect ratio of 1:5 are initially assumed for both fluids and optimized at

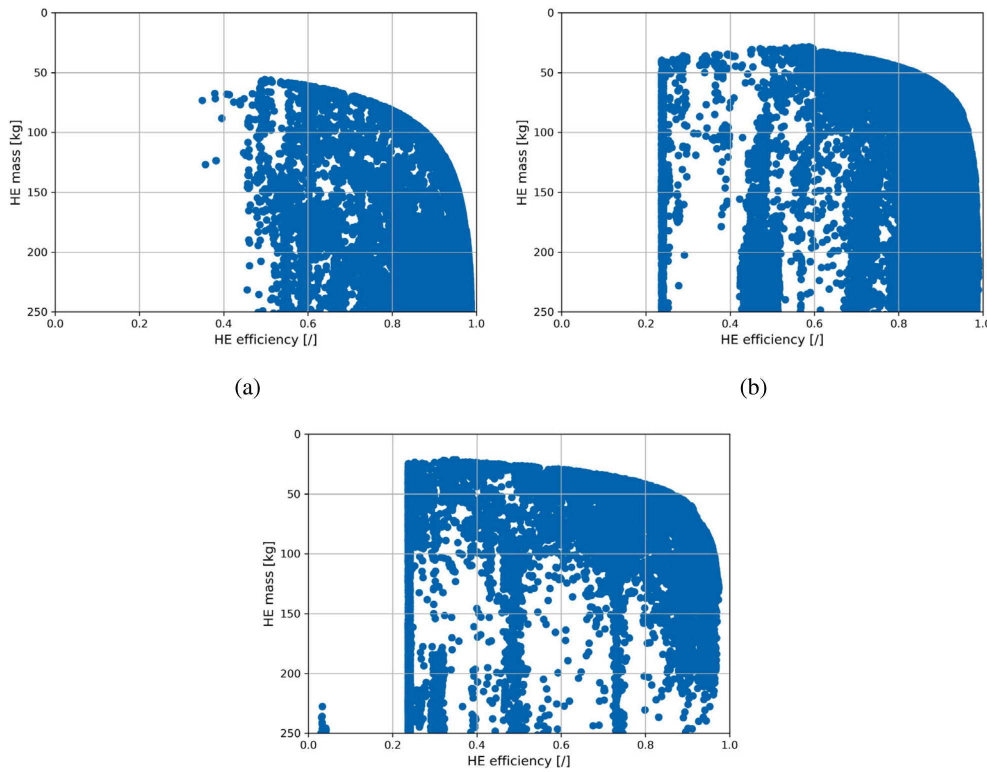

Fig. 8. Multi-objective optimization results for a HE with rectangular channels with a maximum aspect ratio of 1:5 on both fluid sides. Trade-offs between mass minimization and thermal effectiveness maximization for: 8(a) $10\,\mathrm{m\,s^{-1}}$ inlet airspeed, 8(b) $25\,\mathrm{m\,s^{-1}}$ inlet airspeed, and 8(c) $36\,\mathrm{m\,s^{-1}}$ inlet airspeed.

airspeeds of $10\,\mathrm{m\,s^{-1}}$, $25\,\mathrm{m\,s^{-1}}$, and $36\,\mathrm{m\,s^{-1}}$. Fig. 8 collects the results of these three optimizations, highlighting an antagonistic trade-off between thermal effectiveness maximization and mass minimization across all scenarios.

Fig. 9 highlights this trade-off by collecting all non-dominated solutions and tracing the corresponding Pareto optimal frontier for each scenario. For completeness, the optimization is extended to some additional channel configurations, including: circular channels on both fluid sides, circular channels on the coolant side combined with rectangular channels (maximum aspect ratio of 1:5) on the air side, square channels (1:1 aspect ratio) on both sides, and rectangular channels of unrestricted aspect ratio on both sides. To improve readability of the Pareto representation, the solution space is limited to a maximum heat exchanger mass of 150 kg, as higher-mass solutions lie outside the region of interest and are omitted for clarity.

No peer-reviewed studies have been identified reporting both certified HE mass and thermal effectiveness for a 100 kW-class air–water heat exchanger. In the absence of such consolidated datasets, a preliminary assessment of the present optimization results is conducted, indicating that the predicted heat exchanger masses are consistent with those of representative industrial products. Manufacturer technical data-sheets for automotive and heavy-duty aluminium radiators report dry masses in the range of approximately 21 kg to 28 kg, as evidenced by the Freightliner Cascadia radiator [90], the VALEO Class 7–8 radiator [91], and the GEN 124 Aluminum Olympia 100 kW generator radiator [92].

By contrast, larger industrial air–water heat exchangers intended for stationary applications exhibit substantially higher masses, including the F&R Products 100K cooling system, reaching 360 kg for the complete packaged unit [93], the Carrier Rental CRS HEX 100 (170 kg) [94], and the Pfannenberg EB 160 WT air–water heat exchanger, reporting a 140 kg dry mass [95]. Although these systems differ in construction, packaging level, and intended application, they collectively indicate that the mass ranges predicted by the present optimization framework are representative of commercially available heat exchangers across both transport and industrial sectors. Accordingly, the HE mass information extracted from this study will be crucial in the near future development for modular powertrain development in transport applications. The proposed methodology addresses this issue and introduces weight information on new propulsions system design.

Fig. 9 highlights improved performance of solutions at higher air inlet velocities, in agreement with the expected physical behaviour. Fig. 10 further investigates this trend by presenting interpolated performance maps derived from the three simulated airspeeds for four representative channel geometries: circular, square, rectangular with a maximum aspect ratio of 1:5, and rectangular with unrestricted aspect ratio. Also in this case, the representation is truncated to a maximum heat exchanger mass of 150 kg to improve readability and clarity.

These maps provide additional insight into the influence of airspeed, heat exchanger mass, and effectiveness for the assumed design space, highlighting the trends identified from the Pareto fronts in Fig. 9. The hatched regions indicate extrapolated areas outside the simulated airspeed range ($10\,\mathrm{m\,s^{-1}}$ to $36\,\mathrm{m\,s^{-1}}$), and should be interpreted with caution. All four maps exhibit consistent trends, with increasing air velocities improving the attainable thermal effectiveness-to-mass trade-off, albeit with diminishing returns at higher airspeeds. In particular,

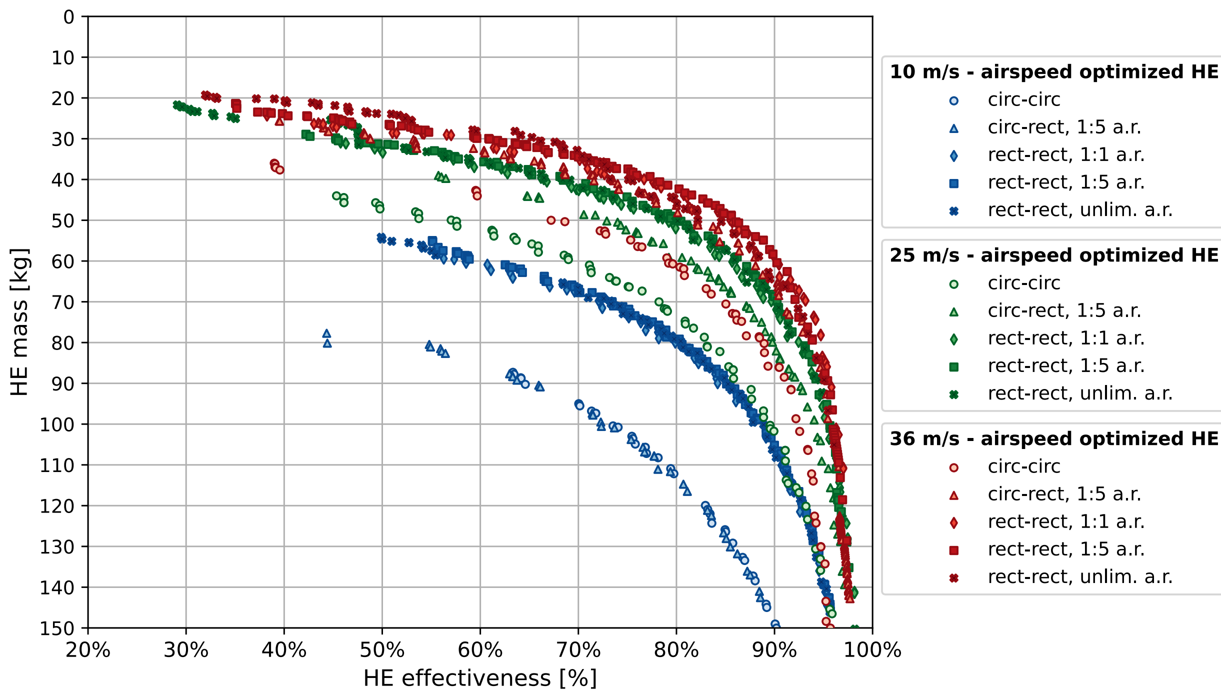

Fig. 9. Pareto frontiers for mass minimization and thermal effectiveness maximization in compact heat exchangers invested by $10\,\mathrm{m\,s^{-1}}$, $25\,\mathrm{m\,s^{-1}}$, and $36\,\mathrm{m\,s^{-1}}$ airspeeds. Comparison between five different channel shape configurations: circular-circular, circular-rectangular (1:5 max aspect ratio), square-square (1:1 max aspect ratio), rectangular-rectangular (1:5 max aspect ratio, both), and rectangular-rectangular (unrestricted max aspect ratio).

increasing the airspeed from $10\,\mathrm{m\,s^{-1}}$ to $25\,\mathrm{m\,s^{-1}}$ produces the largest performance improvements, whereas a further increase to $36\,\mathrm{m\,s^{-1}}$ yields comparatively smaller benefits. At lower airspeeds, increases in thermal effectiveness can only be achieved at the expense of substantial mass penalties, whereas higher airspeeds enable comparable performance improvements with significantly smaller mass increases. For instance, increasing the thermal effectiveness from 40% to 50% requires less than $5\,\mathrm{kg}$ of additional heat exchanger mass at $36\,\mathrm{m\,s^{-1}}$, compared with nearly $10\,\mathrm{kg}$ at $10\,\mathrm{m\,s^{-1}}$. These results provide quantitative insight into how simultaneously maximizing thermal performance while minimizing heat exchanger mass becomes progressively more challenging as the available inlet air velocity decreases.

Results from Fig. 9 also demonstrate that rectangular channel geometries consistently outperform both circular and hybrid configurations, independently of the imposed maximum aspect ratio constraint. To better visualize and quantify this trend, all non-dominated solutions are grouped into six thermal effectiveness intervals of progressively decreasing width, accounting for the asymptotic behaviour of the Pareto front as the thermal effectiveness approaches unity ($\varepsilon \rightarrow 100\%$). For each interval, the corresponding range of heat exchanger masses is determined, enabling a statistical comparison of the five channel configurations, as presented in Fig. 11 for a reference air inlet velocity of $25\,\mathrm{m\,s^{-1}}$.

In Fig. 11, rectangular channel geometries are shown to consistently achieve average masses approximately 33% lower than fully circular configurations of comparable thermal effectiveness. This corresponds to a minimum mass reduction of about $15\,\mathrm{kg}$ for the lightest designs. Compared with hybrid configurations employing circular coolant channels and rectangular air channels, the average mass reduction from employing fully rectangular layouts decreases to approximately 13%. However, this advantage is more pronounced for lighter heat exchangers, reaching up to 16% mass savings (around $6\,\mathrm{kg}$), and gradually decreasing to approximately 11% for bulkier designs exceeding a thermal effectiveness of 85%. This behaviour is primarily attributed to the more efficient use of structural material in rectangular geometries, whereas circular channels require thicker fin roots, resulting in increased material volume per channel and higher overall heat exchanger mass.

Results from Fig. 11 confirm negligible performance differences among the various optimized rectangular geometries, with an average deviation of only 2.7%, regardless of the applied constraints on the maximum allowable aspect ratio. This outcome indicates a substantial performance overlap across rectangular designs over a wide range of solutions, as also observed in Fig. 9, suggesting that, in most cases, moderate aspect ratios compatible with the three rectangular configurations are sufficient. However, a clear distinction emerges, as only configurations with unbounded aspect ratios achieve the lowest recorded mass of $21.7\,\mathrm{kg}$ at a minimum thermal effectiveness of 29.1% (Fig. 11(a)). These findings suggest that extreme aspect ratios, significantly exceeding the 1:5 threshold, are required when targeting the lowest attainable component masses. This trend is further corroborated by the optimized dimensions reported in Table 7, particularly on the hot-fluid side.

4.3. Design selection and export model results

A complete characterization and export of each optimized design is rendered computationally prohibitive by the large number of non-dominated solutions obtained from optimizations across different channel geometries and reference airspeeds. To address this issue, the multi-objective optimization problem is scalarized following Garcia et al. [44]. However, rather than adopting the linear scalarisation originally proposed by the authors, Chebyshev scalarisation is employed instead, enabling improved control over the selection of non-dominated solutions independently of the Pareto front shape [96]. Eq. (27) presents the formulation, here reframed as a max–min problem to align with the PyGAD framework, which is based on solution fitness

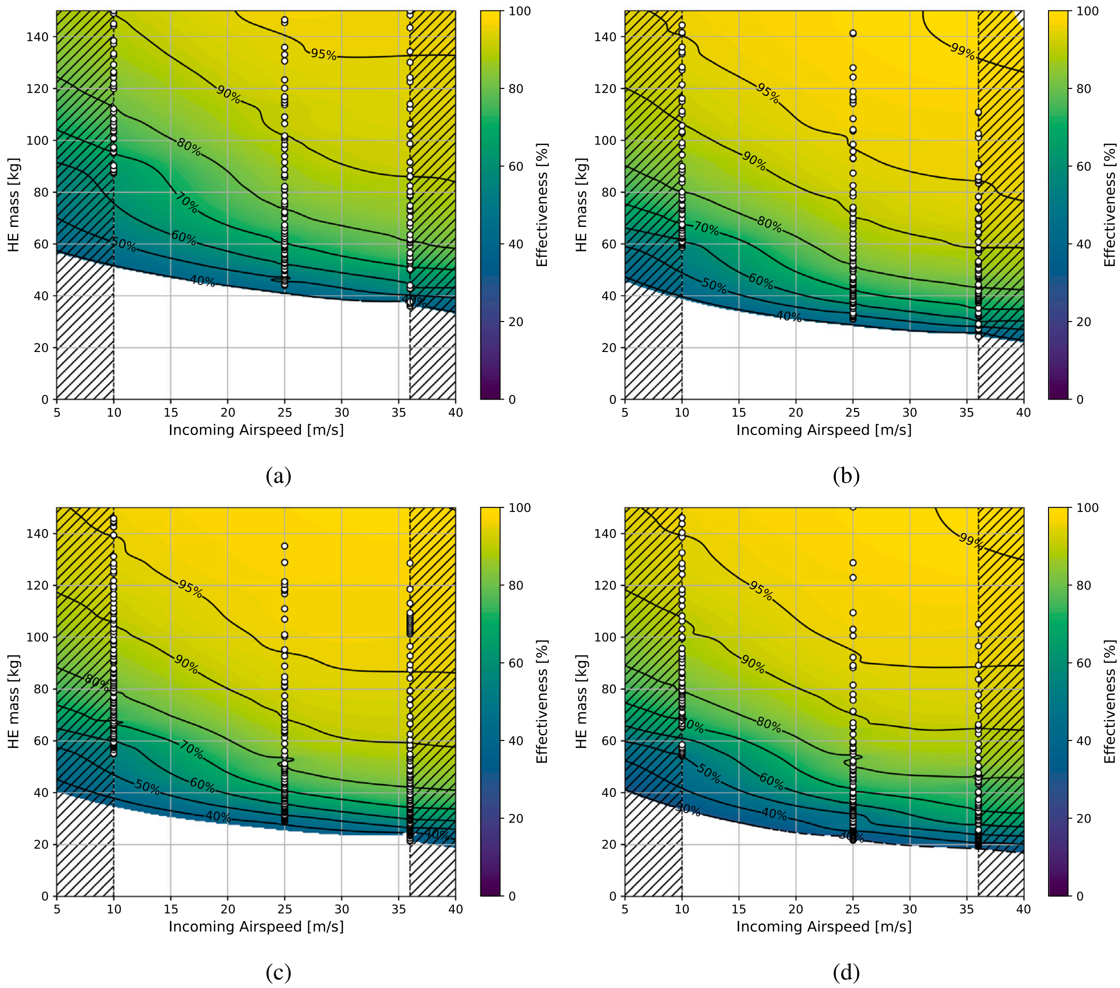

Fig. 10. Performance maps of optimized compact cross-flow heat exchangers at different inlet airspeeds, considering circular 10(a), square 10(b), rectangular with maximum aspect ratio 1:5 10(c), and rectangular with unrestricted aspect ratio 10(d) channel geometries. The surfaces are obtained by interpolation of the simulated airspeed conditions. Hatched regions indicate extrapolated areas outside the simulated airspeed range.

maximization rather than conventional cost minimization:

$$f_{Cheb} = \max_{x \in X} \min_{i=1,\ldots,n} \left\{ \frac{f_i'(x)}{q_i} \right\} \qquad \text{with} \quad \sum_{i=1}^{n} q_i = 1, \quad n = 2 \tag{27}$$

By progressively varying the q_1 and q_2 weights applied to the fitness functions of Eqs. (18) and (19) at regular increments of 12.5%, nine representative geometries are extracted from the Pareto fronts of each optimization. The mass, thermal effectiveness, and volume of the selected solutions are reported in Table 6, keeping the reference $25\,\mathrm{m\,s^{-1}}$ airspeed case.

Notably, several designs obtained through mass-minimization weights ranging from 100% to 62.5% converge to identical solutions. This behaviour arises from the adopted Chebyshev scalarisations, which partition the objective space shown in Fig. 9 into nine angularly distributed reference directions, each associated with a distinct combination of scalarisation weights, which returns the closest feasible Pareto solution. However, since most Pareto fronts in Fig. 9 do not include solutions with thermal effectiveness below 40%, scalarisations assigning low emphasis to thermal performance all converge to the same feasible Pareto-optimal point, causing multiple scalarized functions to collapse onto a single non-dominated solution. Consequently, only six to eight distinct optimized solutions are typically obtained from the scalarisation procedure.

Results from Table 6 also indicate that circular channels enable more compact heat exchanger designs than rectangular ones, despite exhibiting higher component mass, with total volume reductions ranging from 10% to 20%. This behaviour likely stems from their smaller cross-flow area, which increases local velocities and, in turn, enhances Reynolds and Nusselt numbers, leading to higher overall heat transfer coefficients U_{plt} per plate. Accordingly, the required heat transfer area $W_{plt}L_{plt}$ per plate is reduced, resulting in lower overall component volume. This effect is further amplified when compared with rectangular channels of unconstrained aspect ratio, which result in the higher overall HE volumes, as illustrated in Fig. 12.

Notably, combining circular coolant-side ducts with rectangular air-side channels yields the lowest overall volumes, as shown in Table 6 and Fig. 12. These hybrid configurations achieve up to a 30% volume reduction relative to fully rectangular designs while still maintaining lower mass than fully circular ones. This behaviour indicates that reducing channel mass is particularly effective on the gaseous side of the heat exchanger, since the low density of air makes the replacement of solid material with fluid highly impactful on the total component mass. Conversely, the use of circular ducts on the coolant-side offsets the

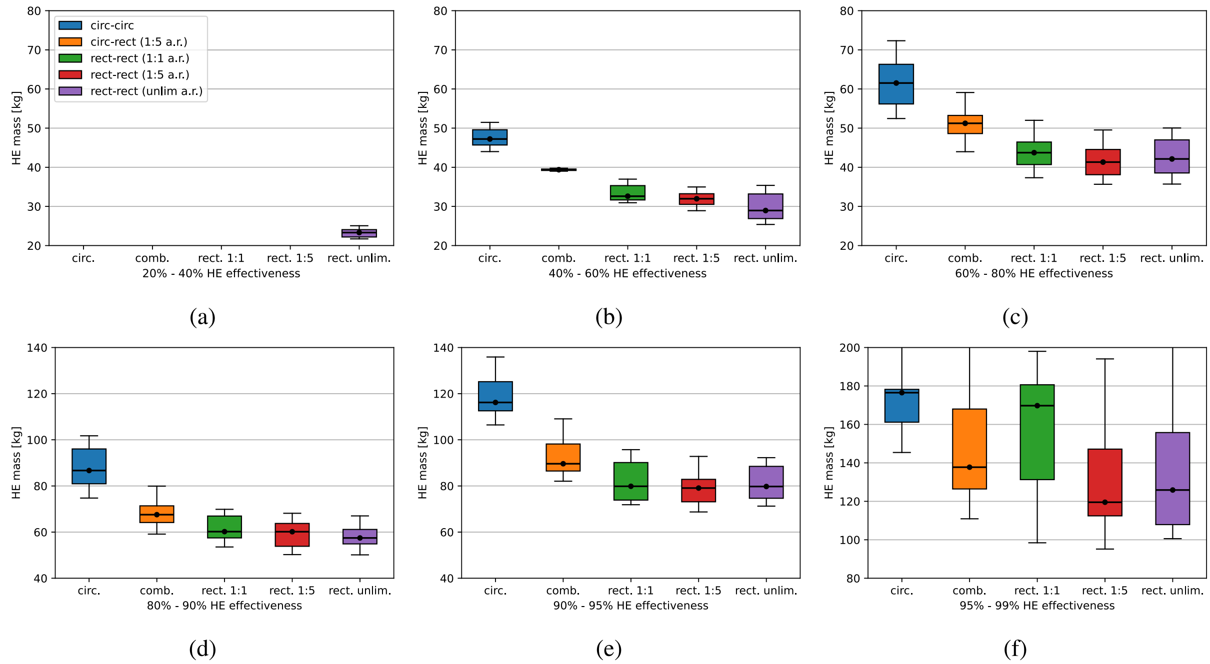

Fig. 11. Multi-objective optimization results of HE assuming $25\,\mathrm{m\,s^{-1}}$ inlet airspeed, and comparison between the following channel shape configurations: circular–circular, circular–rectangular (1:5 max aspect ratio), square–square (1:1 max aspect ratio), rectangular–rectangular (1:5 max aspect ratio, both), and rectangular–rectangular (unrestricted max aspect ratio). Discretization into thermal effectiveness-based bands of: 11(a) 20% to 40% ϵ, 11(b) 40% to 60% ϵ, 11(c) 60% to 80% ϵ, 11(d) 80% to 90% ϵ, 11(e) 90% to 95% ϵ, 11(f) 95% to 99% ϵ.

Table 6
Multi-objective optimization results for HE assuming $25\,\mathrm{m\,s^{-1}}$ inlet air-speed. Details of masses, volumes, and thermal effectiveness of 9 heat exchangers best matching different combinations of desired optimization targets, as extracted from the Pareto fronts. Confront between the following hot-cold channels shape combinations: circular–circular, circular–rectangular (1:5 max aspect ratio), rectangular–rectangular (1:1 max aspect ratio), rectangular–rectangular (1:5 max aspect ratio), and rectangular–rectangular (unbounded max aspect ratio).

ϵ - fitness function weight Mass - fitness function weight		**0%** **100%**	12.5% 87.5%	25% 75%	37.5% 62.5%	**50%** **50%**	62.5% 37.5%	75% 25%	87.5% 12.5%	**100%** **0%**
Hot - Circular Cold - Circular	ϵ [/]	45.3	45.3	45.3	45.3	57.6	71.3	85.8	96.4	99.0
	Mass [kg]	44.0	44.0	44.0	44.0	51.5	62.0	86.5	155.1	352.9
	Vol. [dm^2]	13.0	13.0	13.0	13.0	14.7	18.0	25.4	45.1	112.4
Hot - Circular Cold - Rectangular (1:5 aspect ratio)	ϵ [/]	55.7	55.7	55.7	55.7	65.9	78.6	89.7	97.9	99.1
	Mass [kg]	39.0	39.0	39.0	39.0	44.7	56.1	78.8	158.2	284.6
	Vol. [dm^2]	13.3	13.3	13.3	13.3	15.1	18.9	26.6	56.1	115.8
Hot - Rectangular Cold - Rectangular (1:1 aspect ratio)	ϵ [/]	45.8	45.8	45.8	55.1	71.0	81.8	92.5	98.2	99.1
	Mass [kg]	30.9	30.9	30.9	35.8	42.5	53.9	79.9	150.3	231.4
	Vol. [dm^2]	14.2	14.2	14.2	16.2	19.3	23.8	36.4	67.2	117.3
Hot - Rectangular Cold - Rectangular (1:5 aspect ratio)	ϵ [/]	42.2	42.2	42.2	57.4	71.1	83.7	92.9	97.9	98.4
	Mass [kg]	28.9	28.9	28.9	34.4	41.4	54.6	79.5	147.4	194.1
	Vol. [dm^2]	14.2	14.2	14.2	16.9	20.1	26.5	39.2	75.8	107.0
Hot - Rectangular Cold - Rectangular (unlim. aspect ratio)	ϵ [/]	29.1	29.1	46.6	56.5	71.7	82.6	92.8	98.2	99.0
	Mass [kg]	21.7	21.7	26.7	34.9	42.3	53.5	79.4	150.3	223.8
	Vol. [dm^2]	12.1	12.1	13.9	17.7	21.8	27.6	38.7	76.2	116.0

mass penalty through improved thermal performance, increasing heat transfer effectiveness sufficiently to reduce the required heat transfer area and the resulting component volume.

These results from Table 6 ultimately suggest that rectangular channels are preferable when mass minimization is the primary design objective. By contrast, combined rectangular–circular configurations provide a favourable trade-off for applications requiring higher heat exchanger compactness, albeit at the expense of increased mass. Circular-only designs appear less competitive overall, being outperformed by hybrid configurations in terms of volume and rectangular layouts in terms of mass.

To further investigate the design trends emerging from the optimization, Table 7 is introduced, collecting the optimized genes of the nine reference solutions obtained for the fully rectangular configuration with unrestricted channel aspect ratio at an air inlet velocity of $25\,\mathrm{m\,s^{-1}}$.

Concerning the overall HE dimensions, two distinct trends emerge in the optimized exchanger proportions:

- Solutions targeting higher thermal effectiveness exhibit large coolant inlet areas and smaller air frontal sections, favouring elongated air channels surrounded by nearly stagnant hot coolant. From a conceptual and geometrical perspective, these layouts

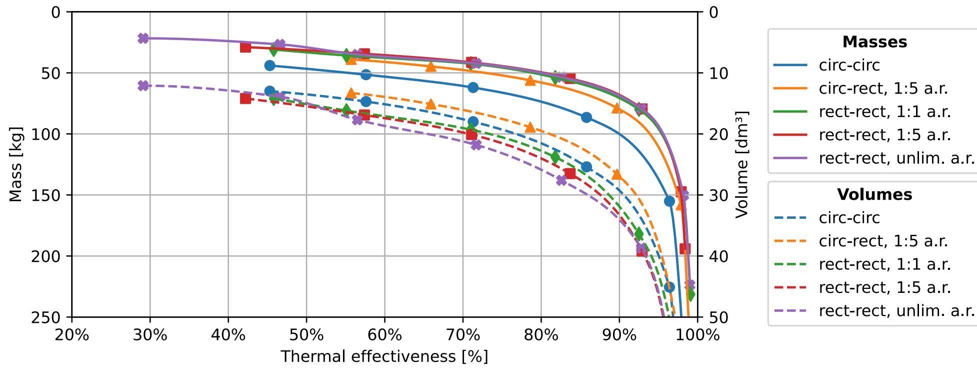

Fig. 12. HE mass to effectiveness and volume to effectiveness trends for the 9 reference HE selected following multi-objective scalarisation. Detail of non-dominated solutions selected according to the following ϵ - mass optimization weights combinations: 0%–100%, 12.5%–87.5%, 25%–75%, 37.5%–62.5%, 50%–50%, 62.5%–37.5%, 75%–25%, 87.5%–12.5%, 100%–0%.

Table 7
Multi-objective optimization results for HE assuming $25\,\mathrm{m\,s^{-1}}$ inlet air-speed and rectangular shaped channels with an unlimited maximum aspect ratio. Details of several geometrical parameters of 9 heat exchangers best matching different combinations of desired optimization targets, as extracted from the Pareto fronts.

ϵ - fitness function weight Mass - fitness function weight	**0%** **100%**	12.5% 87.5%	25% 75%	37.5% 62.5%	**50%** **50%**	62.5% 37.5%	75% 25%	87.5% 12.5%	**100%** **0%**
Number of plates	154	154	118	331	281	242	229	307	307
HE height H_{HE} [mm]	400	400	260	704	598	515	488	717	717
HE hot side length $L_{HE,hot}$ [mm]	30	30	56	85	134	196	308	640	981
HE cold side length $L_{HE,cold}$ [mm]	999	999	960	295	272	273	257	166	165
Inner plate wall height [mm]	0.16	0.16	0.16	0.16	0.16	0.16	0.16	0.16	0.16
Hot fluid channels per plate	1	1	1	1	4	4	81	231	672
Hot fluid channels height H [mm]	1.33	1.33	0.93	0.86	0.86	0.86	0.86	0.86	0.86
Hot fluid channels base B [mm]	29.97	29.97	55.51	83.77	33.34	48.77	3.64	2.60	1.29
Hot fluid fins thickness B_{fin} [mm]	0.17	0.17	0.17	0.71	0.17	0.17	0.17	0.17	0.17
Cold fluid channels per plate	548	548	527	164	149	152	143	91	43
Cold fluid channels height H [mm]	0.94	0.94	0.94	0.94	0.94	0.94	0.94	1.15	1.15
Cold fluid channels base B [mm]	1.66	1.66	1.66	1.64	1.66	1.64	1.64	1.66	3.67
Cold fluid fins thickness B_{fin} [mm]	0.16	0.16	0.16	0.16	0.16	0.1	0.16	0.16	0.16

resemble industrial shell-and-tube heat exchangers or immersion-cooling systems.

- Conversely, solutions prioritizing mass minimization favour smaller coolant inlet areas and larger air frontal sections, promoting shorter and more numerous air channels surrounded by faster-moving hot coolant. These proportions are more characteristic of conventional transport radiators.

Nonetheless, all optimizations consistently minimize both wall and fin thicknesses, indicating that smaller internal features would be desirable if manufacturable, highlighting the importance of reducing laser melting pool dimensions for AM to become more competitive with conventional processes. The only exception to this trend is the hot-channel fin thickness corresponding to the 62.5%–37.5% ϵ–mass scalarisation weight combination, although this is likely an outlier. Additionally, Table 7 also evidences a clear trend of air-side duct minimization, resulting in reduced channel cross-sections and increased number of channels and fins. This pattern indicates that the optimizer systematically aims to increase the wetted surface on the air side of the HE, suggesting that air-side convection constitutes the main bottleneck to heat transfer.

A similar increase in channel count is also observed on the coolant side, albeit only for solutions prioritizing thermal effectiveness. As the optimization shifts towards mass minimization, fewer ducts are favoured instead, with increasingly elongated cross-sections. This behaviour is likely driven by the progressive removal of fins, which the optimizer replaces with coolant volume in an effort to reduce the overall HE mass. The effectiveness of this strategy, however, is strongly dependent on the maximum allowable coolant-channel aspect ratio, forcing square (1:1) duct configurations to rely on alternative adaptations to approach the performance of unrestricted rectangular designs. These geometric adaptations are illustrated in Fig. 13, which compares the overall HE height, length, and depth of the optimized solutions across the three rectangular channel configurations, highlighting how different channel shapes affect the optimized HE envelope proportions.

Results from Fig. 13(a) illustrate that all rectangular configurations exhibit comparable trends for the hot-side overall width, which is maximized to enhance thermal effectiveness and reduced to favour mass minimization. By contrast, the cold-side base width is smaller when thermal effectiveness is prioritized and larger when pursuing mass minimization. This second trend is also noticeably more pronounced in solutions with higher allowable aspect ratios (unbounded). Conversely, designs constrained to a 1:1 aspect ratio tend to maintain smaller cold-side lengths even when minimizing mass, favouring taller configurations instead, composed of a larger number of plates, as shown in Fig. 13(b).

For the purpose of this study, pure thermal-hydraulic-gravimetric optimizations are assumed, while no considerations are made regarding the structural integrity of the obtained designs, which are left for future analyses.

4.4. Dynamic simulation results

Results from Fig. 9 highlight the rectangular channels as the best performing geometries according to the objective functions in Eqs. (18) and (19). Among the proposed configurations, the design with a maximum channel aspect ratio of 1:5 is selected for further analysis to preserve design flexibility while also avoid excessively elongated duct

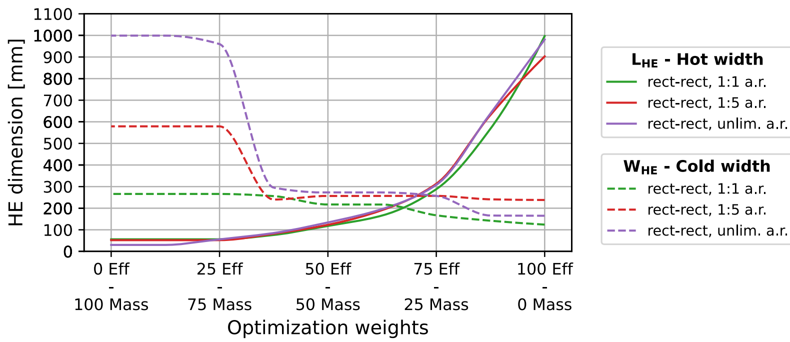

(a)

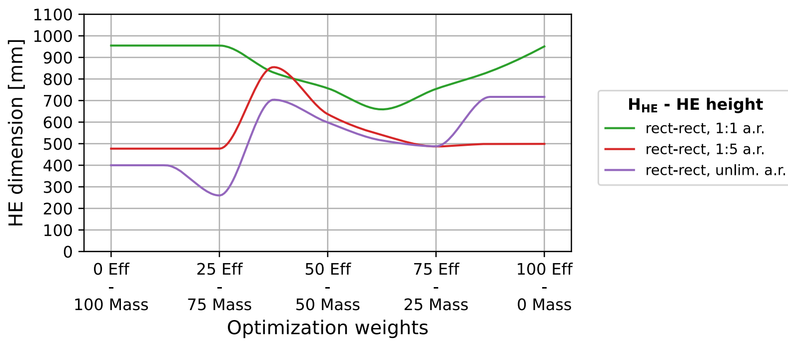

(b)

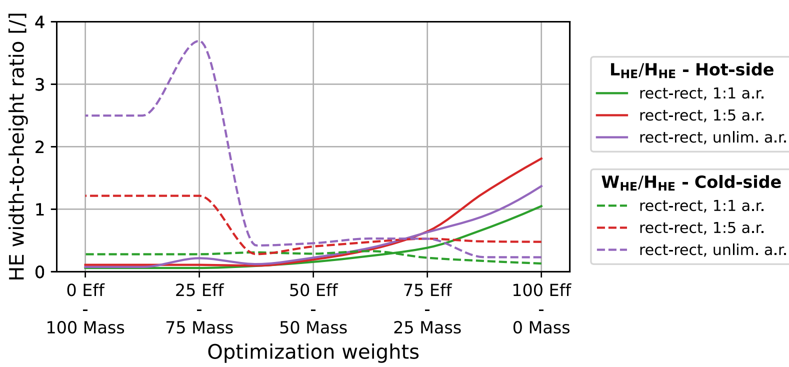

(c)

Fig. 13. Main heat exchanger dimension comparison for the nine reference configurations selected through multi-objective scalarisation, assuming rectangular channel geometries with: 1:1 aspect ratio, 1:5 aspect ratio, and unconstrained aspect ratio. The analysis includes: 13(a) hot- and cold-side entrance base length comparison, 13(b) heat exchanger height trends, and 13(c) hot- and cold-side base length-to-height ratio comparison.

geometries. The following section presents the dynamic simulation of nine non-dominated solutions associated with the reference geometry, extracted from the scalarised multi-objective optimization at $10\,\mathrm{m\,s^{-1}}$ and $36\,\mathrm{m\,s^{-1}}$.

First, a dedicated heat load cycle is applied to all non-dominated solutions to verify compliance with the reference WCS conditions specified in Table 4. A ramp profile is assumed, consisting of 100 s of initial zero heat load and airspeed, followed by a 100 s ramp-up to the optimization boundary conditions, and 30 min of sustained maximum load. This cycle is applied for both reference airspeeds, yielding the results shown in Fig. 14. Since no configuration exceeds the upper temperature threshold of 70 °C, all designs result compliant with the specified WCS requirements.

Once verified under WCS conditions, the nine non-dominated solutions are simulated under their respective reference use cases, assuming the heat load, vehicle speed, and altitude profiles defined in Section 3.3.1. Fig. 15 presents the results of these simulations and provides an overview of the maximum coolant temperatures recorded across the different optimized solutions.

In this case as well, all results comply with the maximum temperature threshold of 70 °C, with the automotive and aerospace cases exhibiting significantly lower temperatures overall. This behaviour arises from the discontinuous heat load profiles of both applications and suggests further optimization opportunities aimed at reducing this gap and the associated component oversizing.

Furthermore, substantially higher thermal inertia is observed in solutions primarily optimized for thermal effectiveness. As shown in Table 7, these configurations feature larger component heights and hot-side base lengths, resulting in wider coolant inlet areas. These, in turn, lead to a greater number of channels and increased coolant volume,

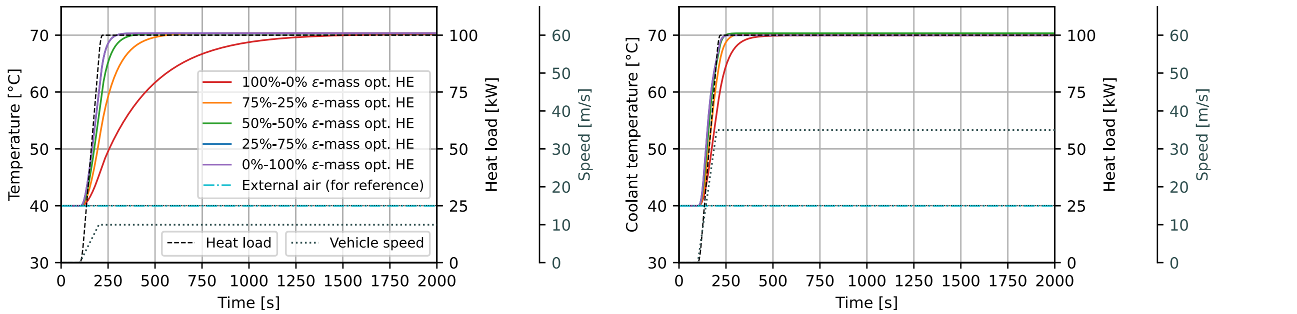

(a) (b)

Fig. 14. Results of the dynamic simulation of several optimized HE geometries with respect to a ramp heat load representing WCS conditions. Detail of non-dominated solutions selected according to the following thermal effectiveness — mass optimization weights combinations: 0%–100%, 25%–75%, 50%–50%, 75%–25%, 100%–0%. 14(a) Dynamic results of HEs optimized for a $10\,\mathrm{m\,s^{-1}}$ air-flow condition. 14(b) Dynamic results of HEs optimized for a $36\,\mathrm{m\,s^{-1}}$ air-flow condition.

which enhances thermal capacity and slows the system's thermal response. This trend is already visible in Fig. 14 and becomes particularly evident for heat exchangers optimized at an airspeed of $10\,\mathrm{m\,s^{-1}}$.

Finally, a preliminary dimensionless CoP is defined and evaluated across the simulations to identify the non-dominated solution that best matches each application. To account for differences among the automotive, aerospace, and marine cases, a generalized CoP is formulated based on variables common to all scenarios, according to Eq. (28):

$$CoP = \frac{1}{t_f - t_0} \int_{t_0}^{t_f} \frac{Q_{HE}}{\frac{\dot{m}_h}{\rho_h} \Delta p_h + m_{HE} \frac{P_{vehicle}}{m_{vehicle}}} dt \tag{28}$$

This metric expresses the system performance as the ratio of exchanged heat to the combined penalties of system mass and pumping power. Specifically, $\frac{\dot{m}h}{\rho_h} \Delta p_h$ represents the instantaneous coolant pumping power, while $mHE \frac{P_{vehicle}}{m_{vehicle}}$ scales the heat exchanger mass with respect to the vehicle power-to-weight ratio, ensuring dimensional consistency between contributions, while capturing the impact of the component mass on the overall vehicle power balance.

Ultimately, the COP is integrated over the mission profile and normalized with respect to the total virtual simulation time to obtain a single scalar performance indicator.

Fig. 16 presents the normalized COPs of all non-dominated solutions for each reference case: automotive and aerospace at $36\,\mathrm{m\,s^{-1}}$, and marine at $10\,\mathrm{m\,s^{-1}}$. The results are further normalized to unity to facilitate comparison between the configurations and highlight the optimization weight combinations yielding the highest COP values, which are then associated with the corresponding Pareto-optimal solutions.

Fig. 16 shows that solutions favouring mass minimization over thermal effectiveness are better suited for automotive and aerospace applications. In both cases, non-dominated solutions optimized at $36\,\mathrm{m\,s^{-1}}$ yield approximately 23.9% higher COP when using a 25%–75% weighting compared to a 37.5%–62.5% weighting. These results are consistent with expectations for aircraft applications, where mass minimization is critical. However, the use of AISI 316 stainless steel may have biased the results towards lighter designs due to the high density of the material and its relatively low thermal conductivity compared with aluminium-based alloys commonly used in industry.

In contrast, geometries obtained with a balanced 50%–50% scalarisation weighting are better suited for marine applications, providing a 1.9% higher COP compared to a 37.5%–62.5% case and an 11.7% increase relative to a 62.5%–37.5% weighting. The lower power-to-weight ratio of maritime systems is the main driver of this shift, indicating that mass minimization is less critical for seagoing applications.

Solutions promoting higher thermal effectiveness, such as those weighted 62.5%–37.5% and above, exhibit lower COP values across all applications and are therefore not competitive for transport applications. As thermal effectiveness approaches unity, diminishing returns are observed, with significant increases in component mass being required for marginal improvements in the thermal performance, as shown in Fig. 9. For instance, increasing a $36\,\mathrm{m\,s^{-1}}$ non-dominated solution from 85% to 90% thermal effectiveness requires an increase in mass from $57.6\,\mathrm{kg}$ to $68.7\,\mathrm{kg}$, corresponding to a 19.4% mass penalty for a 5.5% gain in effectiveness. Accordingly, it can be inferred that such incremental gains in thermal performance do not justify the associated increase in system mass for transport cooling applications. Nevertheless, such highly efficient yet heavier designs may still be relevant in applications where mass is a secondary concern, such as refrigeration, manufacturing, or energy production.

5. Conclusions

This study introduces an innovative design optimization framework for the rapid conceptualization and refinement of compact heat exchangers compatible with AM-SLM. Building on the authors' previous work on the thermo-hydraulic modelling of microchannel cross-flow HEs [54], the framework couples a multi-objective NSGA-II algorithm capable of handling up to 10 design variables, with a dynamic simulation model that evaluates non-dominated solutions under realistic use-case scenarios.

The proposed methodology addresses the growing need for application-oriented design optimization in engineering. The approach focuses on achieving system-oriented goals in which optimization target are matched to the specific requirements of the application, instead of enhancing traditional performance metrics such as the $j/f^{1/3}$ ratio. This is achieved through a number of optimization constraints, enforced through penalty formulations that directly affect the objective functions to hinder the selection of designs which violate prescribed heat transfer targets or pressure drop limits. Additionally, the framework enables the full reconfiguration of the component envelope and proportions within a predefined design space, facilitating the generation of geometries tailored to specific operational constraints. Moreover, this approach fully captures the interactions between the fluid mass flow rates and their corresponding velocities under diverse generated cross-flow areas.

The framework is first assessed against a reference literature component, demonstrating up to a 50% weight saving or a 31% heat transfer enhancement following a $15\,\mathrm{min}$ to $20\,\mathrm{min}$ optimization involving 10^5 candidate geometries. Subsequently, the methodology is applied to the nominal case study of a $100\,\mathrm{kW}$ AISI 316 heat exchanger, optimized against three reference airspeeds: $10\,\mathrm{m\,s^{-1}}$, $25\,\mathrm{m\,s^{-1}}$, and $36\,\mathrm{m\,s^{-1}}$. It returns the key design trade-offs between mass minimization and thermal effectiveness maximization across five channel configurations: circular, circular–rectangular, square, rectangular with a maximum aspect ratio

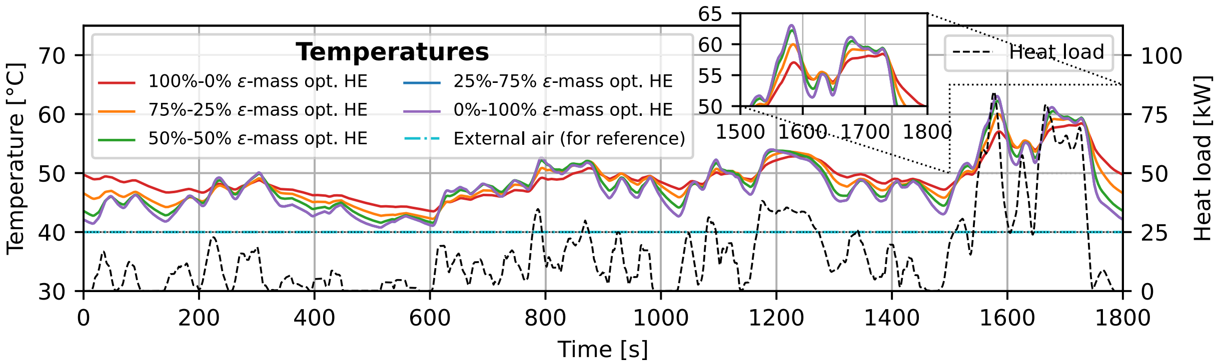

(a)

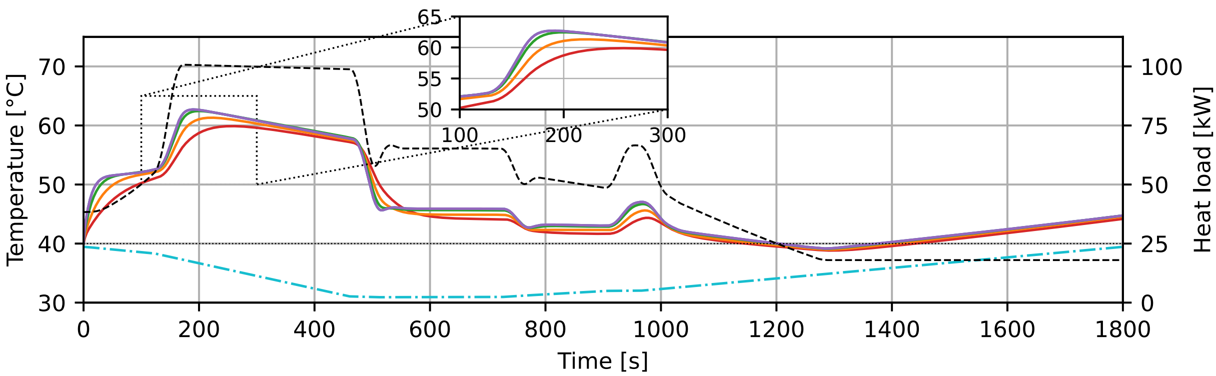

(b)

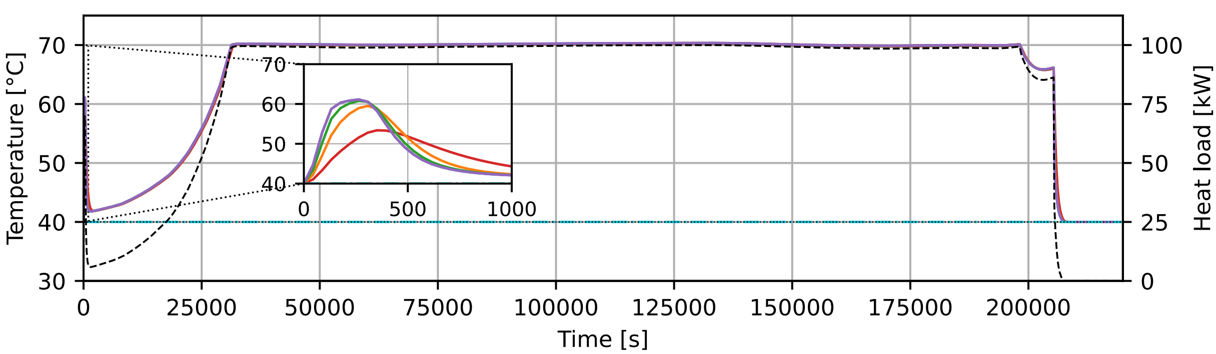

(c)

Fig. 15. Maximum coolant temperatures of five reference heat exchangers adopting rectangular channels geometries with a maximum aspect ratio of 1 : 5. Detail of non-dominated solutions selected according to the following thermal effectiveness — mass optimization weights combinations: 0%–100%, 25%–75%, 50%–50%, 75%–25%, 100%–0%. Simulation results for: 15(a) The third iteration of an automotive heat load cycle based on the WLTP. 15(b) An aerospace heat load profile based on the EASA-FTP-01-00 general aviation reference flight test. 15(c) A generic marine application heat load profile based on predefined AMESIM navigation data and normalized to a reference 100 kW cooling unit.

of 1:5, and rectangular with unconstrained aspect ratio. The main findings are summarized as follows:

1. The two optimization objectives exhibit strongly antagonistic behaviour, with non-dominated solutions approaching unit thermal effectiveness ($\varepsilon \rightarrow 1$) only at the expense of increasingly severe mass penalties;
2. The rectangular channels consistently produce the lightest HE designs overall (down to a minimum of 21.7 kg), reducing component mass by 33% relative to circular ducts and 13% relative to combined circular–rectangular configurations. By contrast, circular ducts exhibit 10%–20% smaller overall volumes than rectangular designs at comparable thermal effectiveness, while hybrid circular–rectangular configurations achieve up to 30% volume reductions. Rectangular geometries are therefore preferable for mass-critical applications, whereas hybrid configurations are better suited for space-constrained designs;
3. Wall and fin thicknesses consistently converge to the lower optimization bound of 160 μm, corresponding to the characteristic AM melting pool diameter. This suggests that further performance gains may be attainable through a reduced manufacturable feature size, where applicable;
4. Rectangular channel geometries consistently favour smaller but more numerous cold-side ducts, indicating that air-side convection constitutes the dominant thermal resistance to the HE. A

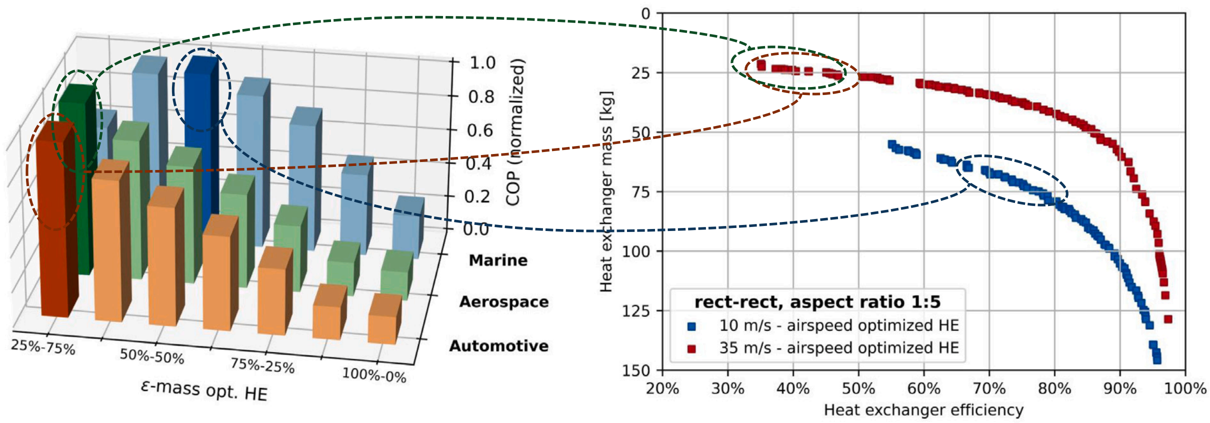

Fig. 16. Normalized CoPs of non-dominated solutions employing rectangular channels with a maximum aspect ratio of 1 : 5. Comparison between the three reference applications: automotive, aerospace, and marine, and identification of the best performing design on the $10\,\mathrm{m\,s^{-1}}$ and $36\,\mathrm{m\,s^{-1}}$ Pareto fronts. Detail of HE designs selected according to the following thermal effectiveness - mass optimization weights combinations: 0%–100%, 12.5%–87.5%, 25%–75%, 37.5%–62.5%, 50%–50%, 37.5%–62.5%, 75%–25%. Optimization weights of 0%–100%, 12.5%–87.5% are neglected since the genetic algorithm converges to identical designs for the 75%–25% weights combination.

similar trend is also observed for the hot-water channels when maximizing thermal effectiveness, whereas elongated channels with high aspect ratios are promoted when aiming for mass minimization;

5. All rectangular-duct configurations exhibit increasing hot-side base lengths with higher thermal effectiveness and decreasing base lengths with mass minimization, whereas the cold-side base lengths follow opposite trends. When the aspect ratio is constrained, as in square and circular ducts, reductions in channel width are compensated by increased component height and number of stacked plates. These results confirm that the internal channel architecture may strongly affect the global geometry of the optimized heat exchanger.

Nine non-dominated solutions are identified via Chebyshev scalarisation of the multi-objective problems and evaluated across three representative applications: an automotive L3H3 van, a general aviation aircraft, and a large marine vessel. Performance is assessed against time-dependent heat-load profiles using a preliminary coefficient of performance (CoP) that accounts for the heat transfer, pumping power, and system power-to-weight ratio of the solution to identify the most suitable design for each application:

- Non-dominated solutions with a thermal effectiveness scalarisation weight of 25% or less achieve the highest CoP for automotive and aerospace applications, indicating that mass minimization is their dominant design driver. However, the use of AISI 316 stainless steel as the reference material may have biased the optimization towards lighter configurations compared to traditional aluminium alloys because of its higher density and lower thermal conductivity;
- A more balanced 50%–50% weighting yields the highest CoP for the marine application instead, suggesting increased thermal performance prominence over mass;
- The solutions that prioritize thermal effectiveness, with scalarisation weights of 62.5% or higher, remain consistently non-competitive across all simulated applications, as the associated mass penalties outweigh the marginal thermal performance gains.

The results of this study outline key trends in the design optimization of AM microchannel heat exchangers. The presented methodology enables extensive design space exploration and rapid component conceptualization for prototyping, introducing mass information related to thermal performance. The moderate computational cost of the tool remains a key enabler for supporting the development of lightweight thermal management systems for future modular propulsion applications.

However, some limitations remain with the current modelling of pressure drops, as the numerical framework relies on a single constant amplification factor K_p to account for pressure drop increase in AM channels. Future work shall aim to address this characterization by introducing refined loss formulations for AM components.

Further developments should also include expanded experimental validation of the optimized designs, together with the investigation of alternative materials and working fluids, such as aluminium alloys, water–glycol mixtures, and humid air. Leveraging the flexible and modular framework of the numerical simulation model, the proposed methodology could also be extended to investigate alternative heat exchanger geometries. Finally, incorporating a dedicated structural mechanics model into the simulation routine represents a clear pathway towards improving the operational feasibility of the optimization outcomes.

CRediT authorship contribution statement

S. Favre: Conceptualization, Methodology, Software, Validation, Formal analysis, Writing - Original Draft, Writing - Review & Editing, Visualization. **D. Di Blasio:** Conceptualization, Methodology, Validation, Formal analysis, Resources, Writing – original draft, Writing – review & editing, Visualization, Supervision. **T. Fletcher:** Conceptualization, Methodology, Resources, Writing – review & editing, Supervision. **E. Brusa:** Conceptualization, Methodology, Resources, Writing – review & editing, Funding acquisition, Supervision. **C. Delprete:** Resources, Writing – review & editing, Supervision.

Funding

This publication is part of the project PNRR-NGEU which has received funding from the MUR - DM352/2022 (CUP n° E12B22000560006).

Declaration of competing interest

The authors declare that they have no known competing financial interests or personal relationships that could have appeared to influence the work reported in this paper.

Appendix. Genes check and validation

The following equations define the corrective transformations applied when translating the chromosomes' genes into the corresponding heat exchanger parameters within the design optimization process. These transformations prevent numerical failures and physical absurd by eliminating incompatible gene combinations that would otherwise lead to infeasible heat exchanger geometries.

Eq. (29) constrains the base length of the HE hot channels to the minimum between the corresponding gene value ($B^{gene}_{chan,h}$) and the heat exchanger base length reduced by twice the fin-wall thickness, thus preventing the channel geometry from extending beyond the physical boundaries of the heat exchanger:

$$B_{chan,h} = \min\left(B^{gene}_{chan,h},\ L^{gene}_{HE,h} - 2B_{fin,h}\right) \tag{29}$$

Eq. (30) applies the same correction for the cold side of the HE:

$$B_{chan,c} = \min\left(B^{gene}_{chan,c},\ L^{gene}_{HE,c} - 2B_{fin,c}\right) \tag{30}$$

Conversely, Eq. (31) prevents incompatible gene combinations from generating plate geometries whose total height exceeds that of the heat exchanger:

$$\begin{cases} H_{chan,h} = \min\left(H^{gene}_{chan,h},\ \frac{H^{gene}_{HE}}{n-1} - nH_w\right) \\ H_{chan,c} = \min\left(H^{gene}_{chan,c},\ \frac{H^{gene}_{HE}}{n-1} - nH_w\right) \end{cases} \tag{31}$$

where $n = 3$ when the two fluids occupy an equal number of layers and $n = 4$ otherwise.

Eq. (32) defines the maximum number of channels that can be accommodated within a plate module for a given heat exchanger base length, ensuring that channel rows do not exceed the available plate width:

$$\begin{cases} n_{h,plt,chan} = \frac{L^{gene}_{HE,h} - B_{fin,h}}{B_{chan,h} + B_{fin,h}} \\ n_{c,plt,chan} = \frac{L^{gene}_{HE,c} - B_{fin,c}}{B_{chan,c} + B_{fin,c}} \end{cases} \tag{32}$$

The inverse form of Eq. (32) is then used to compute consistent heat exchanger base lengths (L_{HE}) from the resulting numbers of channels, fins, and their corresponding widths, yielding an effective base length that is always less than or equal to its gene value: $L_{HE,h} \leq L^{gene}_{HE,h}$.

Eq. (33) completes the corrective transformations, eliminating the last inconsistency and maximizing the number of plates n_{plt} that can be stacked within the heat exchanger height gene H^{gene}_{HE}:

$$\begin{cases} n_{plt} = \frac{H^{gene}_{HE} - H_w - (H_{chan,h} + H_w)}{H_{chan,h} + 2\cdot H_w + H_{chan,c}} & \text{if } n_{h,layers} > n_{c,layers} \\ n_{plt} = \frac{H^{gene}_{HE} - H_w}{H_{chan,h} + 2\cdot H_w + H_{chan,c}} & \text{if } n_{h,layers} = n_{c,layers} \\ n_{plt} = \frac{H^{gene}_{HE} - H_w - (H_{chan,c} + H_w)}{H_{chan,h} + 2\cdot H_w + H_{chan,c}} & \text{if } n_{h,layers} < n_{c,layers} \end{cases} \tag{33}$$

Also in this case, the inverse form of Eq. (33) is then used to recover a physically consistent heat exchanger height H_{HE}, which is always less than or equal to its gene value: $H_{HE} \leq H^{gene}_{HE}$.

Data availability

Data will be made available on request.

References

[1] S.J. Davis, N.S. Lewis, M. Shaner, S. Aggarwal, D. Arent, I.L. Azevedo, S.M. Benson, T. Bradley, J. Brouwer, Y.-M. Chiang, C.T. Clack, A. Cohen, S. Doig, J. Edmonds, P. Fennell, C.B. Field, B. Hannegan, B.-M. Hodge, M.I. Hoffert, E. Ingersoll, P. Jaramillo, K.S. Lackner, K.J. Mach, M. Mastrandrea, J. Ogden, P.F. Peterson, D.L. Sanchez, D. Sperling, J. Stagner, J.E. Trancik, C.-J. Yang, K. Caldeira, Net-zero emissions energy systems, Science 360 (6396) (2018) Cited by: 1533; All Open Access, Green Open Access.

[2] R.C. Pietzcker, T. Longden, W. Chen, S. Fu, E. Kriegler, P. Kyle, G. Luderer, Long-term transport energy demand and climate policy: Alternative visions on transport decarbonization in energy-economy models, Energy 64 (2014) 95–108, Cited by: 155; All Open Access, Green Open Access.

[3] United Nations, Transforming Our World: The 2030 Agenda for Sustainable Development, Resolution A/RES/70/1, United Nations, New York, 2015, URL https://sdgs.un.org/2030agenda.

[4] European Commission, Sustainable and smart mobility strategy – putting European transport on track for the future, 2020, URL https://transport.ec.europa.eu/transport-themes/mobility-strategy_en.

[5] M. Muratori, T. Kunz, A. Hula, M. Freedberg, U.S. National Blueprint for Transportation Decarbonization: A Joint Strategy to Transform Transportation, Technical Report, U.S. Department of Energy, Office of Energy Efficiency and Renewable Energy, 2023, URL https://rosap.ntl.bts.gov/view/dot/66718.

[6] European Commission, Towards zero emission road transport (2zero) partnership, 2021, URL https://www.2zeroemission.eu/. (Accessed 11 April 2025).

[7] J. Tian, P. Wang, D. Zhu, Overview of Chinese new energy vehicle industry and policy development, Green Energy Resour. (ISSN: 2949-7205) 2 (2) (2024) 100075.

[8] Zero Emissions Ship Technology Association (ZESTAs), ZESTAs official website, 2025, URL https://zestas.org/, (Accessed 11 April 2025), Homepage.

[9] European Commission, Zero emission waterborne transport (ZEWT) partnership, 2021, URL https://www.waterborne.eu/partnership/partnership. (Accessed 11 April 2025).

[10] U.S. Maritime Administration, Clean ports program overview, 2023, https://www.epa.gov/ports-initiative/cleanports#about. (Accessed 11 April 2025).

[11] S. Chen, C. Miao, Q. Zhang, Understanding the evolution of China's green shipping policies: Evidence by social network analysis, J. Clean. Prod. (ISSN: 0959-6526) 482 (2024) 144204.

[12] Clean Aviation Joint Undertaking, Clean aviation, highlights 2023: Towards disruptive technologies for aircraft by 2035, 2024, http://dx.doi.org/10.2886/0905205, URL https://op.europa.eu/en/publication-detail/-/publication/2db5dc35-76f6-11ef-bbbe-01aa75ed71a1/language-en.

[13] N.A.R.M. Directorate, Sustainable flight national partnership, 2021, URL https://www.nasa.gov/general/sfnp/.

[14] B.C.H. Steele, A. Heinzel, Materials for fuel-cell technologies, Nature (ISSN: 1476-4687) 414 (6861) (2001) 345–352.

[15] Z.P. Cano, D. Banham, S. Ye, A. Hintennach, J. Lu, M. Fowler, Z. Chen, Batteries and fuel cells for emerging electric vehicle markets, Nat. Energy (ISSN: 2058-7546) 3 (4) (2018) 279–289.

[16] S.G. Kandlikar, Z. Lu, Thermal management issues in a PEMFC stack – A brief review of current status, Appl. Therm. Eng. (ISSN: 1359-4311) 29 (7) (2009) 1276–1280, Selected Papers from the 10th UK National Heat Transfer Conference, Edinburgh, Scotland, September 10-11, 2007.

[17] Y. Wang, Q. Gao, G. Wang, P. Lu, M. Zhao, W. Bao, A review on research status and key technologies of battery thermal management and its enhanced safety, Int. J. Energy Res. 42 (13) (2018) 4008–4033.

[18] L. Fan, Z. Tu, S.H. Chan, Recent development of hydrogen and fuel cell technologies: A review, Energy Rep. (ISSN: 2352-4847) 7 (2021) 8421–8446.

[19] S. Favre, F.D. Fede, E. Brusa, C. Delprete, Fuel-based thermal management system architectures and tank temperature evolution models for aviation, in: ICAS Proceedings, 2024, pp. 1–19, URL https://www.scopus.com/inward/record.uri?eid=2-s2.0-85208779797&partnerID=40&md5=786306d3fa0fa80eec4d67216a10b581, Cited by: 1.

[20] S. Favre, F. Di Fede, E. Brusa, C. Delprete, Innovative thermal management systems for fuel cell electric aircraft, Int. J. Mech. Control. 26 (1) (2025) 159–184, Cited by: 0.

[21] D. Jafari, W.W. Wits, The utilization of selective laser melting technology on heat transfer devices for thermal energy conversion applications: A review, Renew. Sustain. Energy Rev. 91 (2018) 420–442.

[22] I. Kaur, P. Singh, State-of-the-art in heat exchanger additive manufacturing, Int. J. Heat Mass Transfer 178 (2021) Cited by: 209.

[23] F. Careri, R.H. Khan, C. Todd, M.M. Attallah, Additive manufacturing of heat exchangers in aerospace applications: a review, Appl. Therm. Eng. (ISSN: 13594311) 235 (2023) 121387.

[24] A. Fawaz, Y. Hua, S. Le Corre, Y. Fan, L. Luo, Topology optimization of heat exchangers: A review, Energy (ISSN: 0360-5442) 252 (2022) 124053.

[25] B. Northcutt, I. Mudawar, Enhanced design of cross-flow microchannel heat exchanger module for high-performance aircraft gas turbine engines, J. Heat Transf. 134 (6) (2012) 061801.

[26] E. Rasouli, E. Fricke, V. Narayanan, High efficiency 3-D printed microchannel polymer heat exchangers for air conditioning applications, Sci. Technol. Built Environ. 28 (3) (2022) 289–306.

[27] S.-M. Lee, K.-Y. Kim, S.-W. Kim, Multi-objective optimization of a double-faced type printed circuit heat exchanger, Appl. Therm. Eng. (ISSN: 13594311) 60 (1) (2013) 44–50.

[28] A.J. Modi, M.K. Rathod, Characterization of thermal and hydraulic performance of Fin-and-Tube heat exchanger using rectangular winglet vortex generator with punched hole, in: WCX SAE World Congress Experience, SAE International, 2020, pp. 1–14, http://dx.doi.org/10.4271/2020-01-1346.

[29] Y.-T. Lee, L.-H. Chien, J. He, C.-Y. Wen, A.-S. Yang, Air side performance characterization of wavy Fin-and-tube heat exchangers having elliptic tubes with large waffle heights, Appl. Therm. Eng. (ISSN: 13594311) 217 (2022) 119220.

[30] H. Arjmandi, P. Amiri, M. Saffari Pour, Geometric optimization of a double pipe heat exchanger with combined vortex generator and twisted tape: A CFD and response surface methodology (RSM) study, Therm. Sci. Eng. Prog. (ISSN: 2451-9049) 18 (2020) 100514.

[31] H.R. Abbasi, E. Sharifi Sedeh, H. Pourrahmani, M.H. Mohammadi, Shape optimization of segmental porous baffles for enhanced thermo-hydraulic performance of shell-and-tube heat exchanger, Appl. Therm. Eng. (ISSN: 1359-4311) 180 (2020) 115835.

[32] S. Sarangi, D. Mishra, H. Ramachandran, N. Anand, V. Masih, L. Brar, Analysis and optimization of the curved trapezoidal winglet geometry in a high-efficiency compact heat exchanger, Int. J. Therm. Sci. (ISSN: 1290-0729) 164 (2021) 106872.

[33] J. Zou, T. Hirokawa, J. An, L. Huang, J. Camm, Recent advances in the applications of machine learning methods for heat exchanger modeling—a review, Front. Energy Res. (ISSN: 2296-598X) Volume 11 - 2023 (2023).

[34] Y. Qiu, T. Vo, D. Garg, H. Lee, C.R. Kharangate, A systematic approach to optimization of ANN model parameters to predict flow boiling heat transfer coefficient in mini/micro-channel heatsinks, Int. J. Heat Mass Transfer (ISSN: 0017-9310) 202 (2023) 123728.

[35] J. Mao, X. Ma, F. Zhao, G. Wang, L. Zhu, Z. Wang, H. Yang, W. Zhang, Z. Zhu, Y. Wei, A novel design to enhance the heat transfer and reduce pressure drop of heat exchangers based on multi-objective optimization, Numer. Heat Transfer B (2025) 1–29.

[36] M. Kleiner, S. Kuehn, K. Haberger, High performance air cooling scheme using ducted microchannel parallel plate-fin heat sinks, in: Proceedings of 1995 IEEE/CPMT 11th Semiconductor Thermal Measurement and Management Symposium (SEMI-THERM), IEEE, San Jose, CA, USA, ISBN: 978-0-7803-2434-3, 1995, pp. 122–130, http://dx.doi.org/10.1109/STHERM.1995.512061, URL http://ieeexplore.ieee.org/document/512061/.

[37] T. Pujol, I. T'Jollyn, E. Massaguer, A. Massaguer, I.R. Cózar, M. De Paepe, Design optimization of plate-fin heat sink with forced convection for single-module thermoelectric generator, Appl. Therm. Eng. (ISSN: 13594311) 221 (2023) 119866.

[38] D. Zhuang, Y. Yang, G. Ding, X. Du, Z. Hu, Optimization of microchannel heat sink with Rhombus Fractal-like units for electronic chip cooling, Int. J. Refrig. (ISSN: 0140-7007) 116 (2020) 108–118.

[39] S. Shuja, Optimal fin geometry based on exergoeconomic analysis for a pin-fin array with application to electronics cooling, Exergy Int. J. (ISSN: 11640235) 2 (4) (2002) 248–258.

[40] J. Culham, Y. Muzychka, Optimization of plate fin heat sinks using entropy generation minimization, IEEE Trans. Compon. Packag. Technol. 24 (2) (2001) 159–165.

[41] A.A. Nagra, F. Han, Q.H. Ling, M. Abubaker, F. Ahmad, S. Mehta, A.T. Apasiba, Hybrid self-inertia weight adaptive particle swarm optimisation with local search using C4.5 decision tree classifier for feature selection problems, Connect. Sci. 32 (1) (2020) 16–36.

[42] H. Lim, U. Han, H. Lee, Design optimization of bare tube heat exchanger for the application to mobile air conditioning systems, Appl. Therm. Eng. (ISSN: 1359-4311) 165 (2020) 114609.

[43] K. Li, J. Wen, Y. Liu, H. Liu, S. Wang, J. Tu, Application of entransy theory on structure optimization of serrated fin in plate-fin heat exchanger, Appl. Therm. Eng. (ISSN: 1359-4311) 173 (2020) 114809.

[44] J.C.S. Garcia, H. Tanaka, N. Giannetti, Y. Sei, K. Saito, M. Houfuku, R. Takafuji, Multiobjective geometry optimization of microchannel heat exchanger using real-coded genetic algorithm, Appl. Therm. Eng. (ISSN: 1359-4311) 202 (2022) 117821.

[45] M.A. Arie, A.H. Shooshtari, V.V. Rao, S.V. Dessiatoun, M.M. Ohadi, Air-Side heat transfer enhancement utilizing design optimization and an additive manufacturing technique, J. Heat Transf. (ISSN: 0022-1481) 139 (3) (2016) 031901.

[46] B.J. Hathaway, K. Garde, S.C. Mantell, J.H. Davidson, Design and characterization of an additive manufactured hydraulic oil cooler, Int. J. Heat Mass Transfer (ISSN: 00179310) 117 (2018) 188–200.

[47] S. Das, E. Rasouli, T. Ziev, N. Lamprinakos, J. Seo, A. Rollett, P. Vaishnav, V. Narayanan, Design and techno economic optimization of an additively manufactured compact heat exchanger for high temperature and high pressure applications, Appl. Therm. Eng. (ISSN: 13594311) 245 (2024) 122778.

[48] B.S. Mekki, J. Langer, S. Lynch, Genetic algorithm based topology optimization of heat exchanger fins used in aerospace applications, Int. J. Heat Mass Transfer (ISSN: 0017-9310) 170 (2021) 121002.

[49] M. Petrovic, K. Fukui, K. Kominami, Numerical and experimental performance investigation of a heat exchanger designed using topologically optimized fins, Appl. Therm. Eng. (ISSN: 1359-4311) 218 (2023) 119232.

[50] H. Moon, K. Boyina, N. Miljkovic, W.P. King, Heat transfer enhancement of Single-Phase internal flows using shape optimization and additively manufactured flow structures, Int. J. Heat Mass Transfer (ISSN: 00179310) 177 (2021) 121510.

[51] H. Moon, D.J. McGregor, N. Miljkovic, W.P. King, Ultra-power-dense heat exchanger development through genetic algorithm design and additive manufacturing, Joule (ISSN: 25424351) 5 (11) (2021) 3045–3056.

[52] F. Feppon, G. Allaire, C. Dapogny, P. Jolivet, Body-fitted topology optimization of 2D and 3D fluid-to-fluid heat exchangers, Comput. Methods Appl. Mech. Engrg. (ISSN: 0045-7825) 376 (2021) 113638.

[53] S. Sun, T.A. Moreira, B. Rankouhi, X. Yu, I.W. Jentz, D.J. Thoma, M.H. Anderson, X. Qian, Topology optimization, additive manufacturing and thermohydraulic testing of high-temperature heat exchangers, Int. J. Heat Mass Transfer (ISSN: 00179310) 242 (2025) 126809.

[54] S. Favre, D. Di Blasio, T. Fletcher, E. Brusa, C. Delprete, Integrated thermo-hydraulic heat exchanger modelling for additive manufacturing optimisation, Appl. Therm. Eng. (ISSN: 1359-4311) 280 (2025) 128446.

[55] M.-B. Vans, Mercedes-Benz eSprinter 314 L3 RWD Electric Van technical brochure, 2024, https://tools.mercedes-benz.co.uk/current/vans/pricelists/esprinter-panel-van.pdf, Battery-electric panel van, L3 length, 100kW electric motor, 81kWh battery.

[56] Textron Aviation / Cessna, Cessna 172 Skyhawk Piston aircraft brochure, 2025, https://cessna.txtav.com/-/media/cessna/files/product-cards/piston/skyhawk_product_card.pdf, Includes performance (range 640nm, cruise 124ktas), useful load, engine specs (Lycoming IO-360-L2A, 180hp), dimensions, avionics (GarminG1000NXi), and field performance:contentReference[oaicite:1]index=1.

[57] A. Tools, NACA 2412 airfoil, 2025, http://airfoiltools.com/airfoil/details?airfoil=naca2412-il. (Accessed 30 June 2025).

[58] W.-M. Wu, The optimal speed in container shipping: Theory and empirical evidence, Transp. Res. E (ISSN: 1366-5545) 136 (2020) 101903.

[59] A. Godet, Prediction of container ships' speed-power relationship for various operational conditions, Transp. Res. Procedia (ISSN: 2352-1465) 72 (2023) 1861–1868.

[60] R. Nacke, B. Northcutt, I. Mudawar, Theory and experimental validation of cross-flow micro-channel heat exchanger module with reference to high Mach aircraft gas turbine engines, Int. J. Heat Mass Transfer (ISSN: 00179310) 54 (5–6) (2011) 1224–1235.

[61] R. Da Silva, M. Mortean, K. De Paiva, L. Beckedorff, J. Oliveira, F. Brandão, A. Monteiro, C. Carvalho, H. Oliveira, D. Borges, V. Chastinet, Thermal and hydrodynamic analysis of a compact heat exchanger produced by additive manufacturing, Appl. Therm. Eng. (ISSN: 13594311) 193 (2021) 116973.

[62] H. Schlichting, Boundary-Layer Theory, Seventh ed., in: McGraw-Hill Classic Textbook Reissue Series, McGraw-Hill, ISBN: 9780070553347, 1979.

[63] F.P. Incropera, D.P. DeWitt, T.L. Bergman, A.S. Lavine, Fundamentals of Heat and Mass Transfer, eighth ed., John Wiley & Sons, Hoboken, NJ, ISBN: 978-1-119-32042-5, 2017.

[64] V. Gnielinski, G1 heat transfer in pipe flow, in: VDI Heat Atlas, Springer Berlin Heidelberg, Berlin, Heidelberg, ISBN: 978-3-540-77877-6, 2010, pp. 691–700, http://dx.doi.org/10.1007/978-3-540-77877-6_34.

[65] V. Gnielinski, On heat transfer in tubes, Int. J. Heat Mass Transfer (ISSN: 0017-9310) 63 (2013) 134–140.

[66] M. Mortean, M. Mantelli, Nusselt number correlation for compact heat exchangers in transition regimes, Appl. Therm. Eng. (ISSN: 1359-4311) 151 (2019) 514–522.

[67] V. Gnielinski, Neue gleichungen für den wärme- und den stoffübergang in turbulent durchströmten rohren und kanälen, Forsch. Ingenieurwesen A (ISSN: 1434-0860) 41 (1) (1975) 8–16.

[68] R.K. Shah, D.P. Sekulić, Fundamentals of Heat Exchanger Design, John Wiley & Sons, Hoboken, NJ, ISBN: 978-0-471-32171-2, 2003.

[69] R.L. Panton, Incompressible flow, in: Incompressible Flow, John Wiley & Sons, Ltd, ISBN: 9781118713075, 2013, pp. 198–219, http://dx.doi.org/10.1002/9781118713075.ch10.

[70] W. Kays, A. London, Compact Heat Exchangers, third ed., Krieger Publishing Company, ISBN: 9781575240602, 1998.

[71] S.W. Churchill, Friction-factor equation spans all fluid-flow regimes, Chem. Eng. 84 (24) (1977) 91–92.

[72] P. Gradl, A. Cervone, P. Colonna, Enhancement of friction factors for microchannels fabricated using laser powder directed energy deposition, Mater. Des. (ISSN: 0264-1275) 251 (2025) 113673.

[73] M. Kadivar, D. Tormey, G. McGranaghan, A review on turbulent flow over rough surfaces: Fundamentals and theories, Int. J. Thermofluids (ISSN: 2666-2027) 10 (2021) 100077.

[74] M.E. Taslim, T. Li, D.M. Kercher, Experimental heat transfer and friction in channels Roughened With Angled, V-Shaped and discrete ribs on two opposite walls, in: Volume 4: Heat Transfer; Electric Power; Industrial and Cogeneration, American Society of Mechanical Engineers, ISBN: 978-0-7918-7886-6, 1994, V004T09A018, http://dx.doi.org/10.1115/94-GT-163, URL https://asmedigitalcollection.asme.org/GT/proceedings/GT1994/78866/The%20Hague,%20Netherlands/245669.

[75] K.A. Thole, S.P. Lynch, A.J. Wildgoose, Chapter Five - Review of advances in convective heat transfer developed through additive manufacturing, in: J.P. Abraham, J.M. Gorman, W. Minkowycz (Eds.), Advances in Heat Transfer, in: Advances in Heat Transfer, Vol. 53, Elsevier, 2021, pp. 249–325, http://dx.doi.org/10.1016/bs.aiht.2021.06.004, URL https://www.sciencedirect.com/science/article/pii/S0065271721000046.
[76] I.H. Bell, J. Wronski, S. Quoilin, V. Lemort, Pure and Pseudo-pure fluid thermophysical property evaluation and the open-source thermophysical property library CoolProp, Ind. Eng. Chem. Res. 53 (6) (2014) 2498–2508.
[77] G.F. Nellis, S.A. Klein, Numerical modeling of cross-flow heat exchangers, in: Heat Transfer, Cambridge University Press, ISBN: 9780521881074, 2008, pp. 919–937.
[78] A.F. Gad, Pygad: An intuitive genetic algorithm python library, Multimedia Tools Appl. (2023) 1–14.
[79] M.M. Company, Automotive and industrial radiators technical datasheet, 2023, URL https://www.modineev.com/products/fuel-cell-stack-cooling-package/. (Accessed 24 June 2025).
[80] V.T. Systems, Thermal management solutions for commercial vehicles, 2021, URL https://www.valeo.com/en/catalogue/ths/front-cooling-modules/. (Accessed 24 June 2025).
[81] K. Kempen, F. Welkenhuyzen, J. Qian, J.-P. Kruth, Dimensional accuracy of internal channels in SLM produced parts, in: Proceedings - ASPE 2014 Spring Topical Meeting: Dimensional Accuracy and Surface Finish in Additive Manufacturing, San Francisco, USA, 2014, pp. 76–79.
[82] P. Minetola, M. Galati, F. Calignano, L. Iuliano, G. Rizza, L. Fontana, Comparison of dimensional tolerance grades for metal AM processes, Procedia CIRP (ISSN: 22128271) 88 (2020) 399–404.
[83] Y. Heynen, R. Liedtke, M. Schier, F. Heckert, Experimental investigation of the influence of climatic conditions and vehicle dynamics on the thermal management system of a fuel cell electric vehicle, Energies (ISSN: 1996-1073) 18 (11) (2025).
[84] M. Asli, P. König, D. Sharma, E. Pontika, J. Huete, K.R. Konda, A. Mathiazhagan, T. Xie, K. Höschler, P. Laskaridis, Thermal management challenges in hybrid-electric propulsion aircraft, Prog. Aerosp. Sci. (ISSN: 0376-0421) 144 (2024) 100967.
[85] Standard atmosphere, 1975.
[86] T. Gillespie, Fundamentals of Vehicle Dynamics, in: Premiere Series Bks, Society of Automotive Engineers, ISBN: 9781560911999, 1992, URL https://books.google.it/books?id=L6xd0nx5KbwC.
[87] European Union Aviation Safety Agency (EASA), Flight Test Programme — EASA-FTP-01-00 (General Aviation / Ultra-light Aircraft), 2016, URL https://www.easa.europa.eu/download/general-aviation/documents-guidance-and-examples/ABCD-FTP-01-00%20-%20Flight%20test%20programme%20-%2017.02.16%20-%20v1.docx, Technical guidance document.
[88] M. Cook, M. Cook, Flight Dynamics Principles: A Linear Systems Approach to Aircraft Stability and Control, in: Aerospace Engineering, Elsevier Science, ISBN: 9780080982427, 2012, URL https://books.google.it/books?id=hgZDmoL4_DcC.
[89] N.G.R. Center, Forces in a climb, 2021, URL https://www.grc.nasa.gov/www/k-12/BGP/climb.html.
[90] Dolphin Heat Exchanger USA, Inc, Freightliner cascadia radiator (product 6601957) – technical specification sheet, 2025, URL https://dolphincatalogue.com/products/6601957, Aftermarket product listing; heavy-duty truck radiator with geometric and construction specifications for Freightliner Cascadia applications.
[91] AUTODOC Marketplace (listing for VALEO), VALEO engine radiator 733537 – technical specifications, 2025, URL https://trucks.autodoc.co.uk/valeo/7065926, Aftermarket catalogue listing referencing original VALEO radiator design; includes dimensional and mass data (810 × 708 × 52 mm, 21 kg). OEM manufacturer: VALEO.
[92] C, G. & J. Inc, GEN 124 aluminum olympia 100 kw generator radiator – technical specification sheet, 2025, URL https://cgj.com/product/gen-124-aluminum-olympia-100kw-generator-radiator, Manufacturer datasheet specifying all-aluminium construction, core dimensions (27.5 × 26.0 × 2.25 in), and dry mass (22.7 kg).
[93] F&R Products Ltd, 100K Cooling System – Technical Data Sheet, Technical Report, F&R Products Ltd., 2018, URL https://fandrproducts.co.uk/wp-content/uploads/2018/05/Technical-Data-Sheet-100K.pdf, Original manufacturer technical datasheet reporting thermal performance, geometry, and total system mass for the 100K cooling unit.
[94] Carrier Rental Systems, Carrier CRS HEX 100 – Technical manual and specifications, 2025, URL https://manuals.plus/m/ede147264113d634166378dddd5881c80feac1fdfc347fbac0ff1458ccbc5afa, Archived technical documentation for Carrier Rental Systems CRS HEX 100 air-water heat exchanger, including dimensional and performance data.
[95] Pfannenberg GmbH, EB 160 WT UL CUS Air/Water Heat Exchanger – Technical Datasheet, Technical Report, Pfannenberg GmbH, 2020, URL https://products.pfannenberg.com/mc-assets/DASSI/TDS_PUBLIC/DataSheet_42031605026_3.0.pdf, Original OEM datasheet reporting cooling capacity, dimensions, and dry mass (weight without fluid) for the EB 160 WT unit.
[96] P. Súkeník, C. Lampert, Generalization in multi-objective machine learning, Neural Comput. Appl. (2024).